IPP-Report

Lier,A.

Kinetic Modeling of Runaway Electron Dynamics

IPP 2018-15
Juni 2018

Technical University Of Munich

Master-Thesis

Kinetic Modeling of Runaway Electron Dynamics

Author:
Andrej Lier

Supervisors:
Prof. Sibylle Günter
Dr. Gergely Papp

June 3, 2018

Abstract

One of the problems that reactor-relevant tokamaks face are plasma terminating disruptions. Under certain circumstances a beam of high energy electrons, so-called *runaway electrons* (REs) can form, which pose serious damage to the plasma facing components. In this thesis I numerically investigate the dynamics of REs using the relativistic, full-f, linearized kinetic (Fokker-Planck) solver CODE ("COllisional Distribution of Electrons") for experimentally relevant scenarios. After a theoretical introduction into the kinetic solver applied here, I apply basic validation, testing and convergence scans.

The first type of experimentally relevant case investigated is a "flat-top" scenario. Here runaways are formed under quiescent (flat-top) parts of a regular tokamak discharge. We were trying to understand if CODE is suitable to model FTU (Frascati Tokamak Upgrade) flat-top cases and provide distributions suitable for experimental comparisons. I made an extensive parameter scan to study the effect of individual plasma parameters on the evolution of the distribution. I have found that simply using the data as supplied would lead to a significant overproduction of REs in the simulation. The experimental discrepancy can possibly be explained by measurement uncertainties or runaway transport in the flat-top scenario due to e.g. turbulence.

The second (and more challenging) application is the case of post-disruption runaway generation for an ASDEX Upgrade (AUG) disruption case. This part of the project requires self-consistent treatment of the electric field, which introduces numerical complications, and makes the calculations significantly slower. I discuss a number of cases where numerical issues were not possible to resolve in the given timeframe. I finally close with a successful calculation for a post-disruptive runaway beam case. This is first time it had been possible to calculate RE generation for an AUG-like disruption using a full-f solver with a self-consistent electric field.

Contents

Acknowledgements

I would like to offer special thanks to my thesis advisor Gergely Papp, who took responsibility for me and guided me through a year of hard work. He was always available and helpful when I ran into trouble and pushed me in the directions necessary. Also I would like to thank Sibylle Günter for taking time to supervise my thesis.

In the end, this work would not have been possible without the existence of CODE, collaboratively written and helpfully provided by Adam Stahl, Gergely Papp, Ola Embréus, Linnea Hesslow, George Wilkie and Mathias Hoppe. It would also not have been possible without FTU Team, in particular Daniele Carnevale and Mateusz Gospodarczyk, who gave me access to their data, stayed in contact and thus allowed me to participate in experimentally relevant events.

Thanks also goes to Lisa Schlüter, my cat, and Konstantin Schweizer for proof-reading and unscrambling my mazy texts, although we might arguably have different "opinions" on where the comma belongs or how long a sentence can be before it becomes Kafkaesque. I am really looking forward to redo that favor. On the other side of the scale, I also greatly appreciate Lisa for allowing me to mentally cool down during my research and enjoy the summer with a nice combination of volleyball, Latin music and Asian food.

1. Introduction

As the world's demand for new and sustainable energy resources grow, innovative methods are searched for in a vast field of possibilities. While renewable energies often directly or indirectly rely on the energy radiated by the Sun, the idea of a fusion reactor is not to harvest but to imitate the physical process of our star. Nuclear fusion is considered to become a substantial energy supplier by the second half of this century [1] due to it being a safe, clean, controlled and affordable way of energy production [2, 3].
At distances, where the attractive strong interaction overcomes the magnitude of the repulsive Coulomb force, light atomic nuclei can unite into another nucleus. Because the average binding energy per nucleon peaks roughly around Iron-56, fusing atoms below that atomic number will usually result in an energy release [4]. In order to overcome the Coulomb barrier, energy for the collisions necessary, can be provided through heat. For this process to be feasible, temperatures have to reach millions of Kelvins, at which point the medium in question is becoming a plasma - an ionized, quasi-neutral gas. Since the cross-section of Coulomb scattering is higher than the fusion cross-section, *confinement* of the fuel plasma is required. Thus the Coulomb interactions mostly redistribute the energy instead of leading to particle and energy loss.
One concept of nuclear fusion currently under research is therefore *magnetic confinement fusion* [2], where the containment of the fuel is provided through magnetic forces. The plasma - being a heavily ionized medium - collectively succumbs to the electromagnetic effects, forcing continuous collisions and therefore enabling fusion to effectively take place. One device concept for magnetic confinement fusion is the so-called *tokamak* [2]. A heated plasma will naturally try to expand. For this reason, the magnetic coils of a tokamak are arranged in a way, that the plasma is kept from physically touching the device wall, as the operative temperatures at the order of 100 million Kelvins would melt any known material and lead to dissipation of energy.

Its' principle shall be explained using figure 1 and the enumeration therein. External toroidal field coils (1) create magnetic field lines (2) along which the charged particles in the plasma can travel. Subsequently, the expansion of the fuel will be dealt with. The basic equation, to which confinement problems in plasma physics come down to, is the equilibrium equation [5]

$$\vec{j} \times \vec{B} = \nabla p.$$

Originating from the magnetohydrodynamic (MHD) equations, forces generated by a current j and a magnetic field B are capable of counteracting a certain

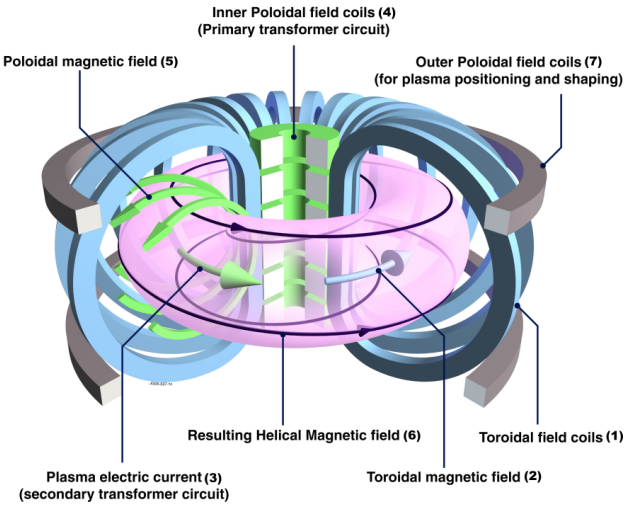

Figure 1: Working principle of a tokamak device.

pressure gradient ∇p. A linearly flowing current will induce a perpendicular magnetic field, which in turn, will pull the conducting material together. In a tokamak, the plasma acts as this conducting material through which an electric current (3) is driven by inner field coils (4), creating poloidal magnetic field lines (5) in the process. The resulting magnetic field line configuration is a helical one (6), carrying plasma inside. Additional outer poloidal field coils (7) can be used to for shaping and positioning purposes. The poloidal magnetic field lines bear another important function: Inherently caused by its geometry, charge dependent particle drift effects appear in a tokamak, separating ions and electrons. Since the thusly created electric field E would cause $E \times B$-drifts to transport the particles outwards, the potential differences have to be dispelled. The poloidal magnetic field allows the separated charges to move along the field lines effortlessly and remove the potential differences (*Pfirsch-Schlüter-currents*). Following each of the helical magnetic field lines, one ends up with a toroidal surface of constant pressure, so-called *flux surfaces*, which, layered together, confine the tokamak plasma.

According to the current state of research, it is to be assumed that sudden losses of plasma confinement in a tokamak can not be ruled out [6]. These so-called *disruptions* occur, when the plasma is on the threshold of its MHD-stability [7, 8]. A quick cooling of the plasma is the consequence of a disruption, dropping its conductivity significantly, and hereby giving rise to a strong self-inducted electric field, capable of damaging the device mechanics through electromagnetic forces. Heat loads of the unconfined plasma onto the plasma-facing components are also a concern for the device [9]. Additionally, as will be explained in the following section, the strong plasma current (orders of Mega Amperes), can be converted in significant fraction into a current carried by so-called *runaway electrons* (REs) [10, 11, 12]. Apart from interfering with the fusion power plant operation, disruptive scenarios and the high energy beam of REs pose a great threat to future devices [13]. Disruption avoidance techniques are currently under development [14, 15].
Runaway electrons require specific controllers to ensure their confinement and/or mitigation techniques to dissipate safely [16]. One technique trying keep REs in check is the *massive material injection* (MMI), which achieves mitigation effects by an increase of the plasma density and by introducing high-Z materials which are detrimental to runaway production. The two main types of MMI are massive gas injection (MGI), where room temperature gas is injected to trigger and mitigate the disruption and runaway generation. This is also the method used on on ASDEX Upgrade, on which the disruption simulations of this thesis are based [17]. The other method currently being tested is shattered pellet injection (SPI), which delivers material in the form of high-speed cryogenic pellets [11, 12].

Analysis of REs requires (a) a kinetic physics model, that will be introduced in section 2 and (b) a numerical solver applied to it, one of which is introduced in section 3. Section 4 and 5 are dedicated respectively to the study of REs in quiescent and disruptive scenarios.

2. Kinetic plasma theory

Kinetic theory in plasma physics is similar to the kinetic description known from thermodynamics with a few distinct additions [5]. A plasma is to be spoken of, when within a quasi-neutral gas the ionization degree is high enough for inner electromagnetic effects to be significant to its behavior. These effects will be considered, when simplifying the *kinetic equation (1)* in order to end up with the so-called *Fokker-Planck equation (2)*, which is the main subject to this thesis.

A certain species of particles a is described using the normalized distribution function $f_a(\mathbf{x}, \mathbf{p}, t)$ in phase-space, denoted respectively by position $\mathbf{x}$ and momentum $\mathbf{p}$. The normalization is chosen such, that $n_s(t, \mathbf{x}) = \int f_a(\mathbf{x}, \mathbf{p}, t)\, \mathrm{d}\mathbf{p}$ is the number density and $N_a(t) = \int n_a(t, \mathbf{x})\, \mathrm{d}\mathbf{x}$ is the total particle number. The distribution function expresses the probability density of finding a particle in the phase-space volume $[\mathbf{i}, \mathbf{i} + \mathrm{d}\mathbf{i}]$ for $\mathbf{i} \in (\mathbf{p}, \mathbf{x})$ at a certain point in time t. The time-evolution of this function is given by the kinetic equation, which reads

$$\frac{df_a}{dt} = \frac{\delta f_a}{\delta t} + \frac{\delta}{\delta \mathbf{x}}(\dot{\mathbf{x}} f_a) + \frac{\delta}{\delta \mathbf{p}}(\dot{\mathbf{p}} f_a) = \sum_b \mathrm{C_{ab}}\{f_a, f_b\} + \mathrm{S}. \tag{1}$$

It contains the time-derivatives $\dot{\mathbf{x}}$ and $\dot{\mathbf{p}}$, both of which will be considered to be influenced by macroscopic forces, such as electric field acceleration and the Lorentz-force. Macroscopic hereby means, that the short-scale fluctuations near the charge-carrying particles themselves are ignored, and electric field $\mathbf{E}$ and magnetic field $\mathbf{B}$ are understood as macroscopically measurable, averaged over many Debye-lengths. The Debye-length is the characteristic length scale, up to which its electrostatic strength is considered unshielded and is given by

$$\lambda_D = \sqrt{\frac{\epsilon_0 k_B T_e}{n_e e^2}}$$

with the vacuum permittivity ϵ_0, the electron temperature T_e and electron charge e, as well as the electron density n_e. From now on, any temperature T will be used as energy measure $E = k_B T$, ignoring the Boltzmann constant k_B. The microscopic fluctuations, shielded on the Debye-length scale, are instead contained in the Boltzmann collision-operator $\mathrm{C_{a,b}}\{f_a, f_b\}$ on the right-hand side of eq. (1), which is often the main origin of complexity (section 2.1). The notation here allows the species of interest a to scatter on all particle species b present in the plasma, including self-collisions. Additional sources (and sinks) of particles and energy can be inclosed in the term S.

Due to its complex nature, eq. (1) has to be simplified for feasible numerical treatment. The main focus of my work is momentum-space dynamics, allowing a 0D approach. This simplification means a complete lack of spatial dimensions, representing a local description of an infinite, homogeneous plasma. 1D calculations with a radial dimension are also possible (see e.g. numerical solver LUKE [18]), but are out of the scope of the present thesis. After simplification, the remaining $f_s(t, \mathbf{p})$ will be represented in a spherical

momentum coordinate system (p, Θ, ϕ), where Θ $[-\pi/2, \pi/2]$ is the longitudinal angle and ϕ $[0, \pi]$ the azimuthal angle in relation to the main direction laid toroidally and antiparallel to the electric field, so the electrons are accelerated in positive direction. In a strong magnetic field of several tesla, as it is present in tokamaks, the gyro motion of charged particles along the magnetic field lines can be averaged over. The gyro radius becomes small (compared to gradients in the plasma) and the gyro time scale is ignorable compared to the thermal collision time, ultimately eliminating the azimuthal angle ϕ. The remaining two momentum-dimensions will be chosen as the normalized momentum $p = \gamma v/c$ and the cosine of the particle pitch $\xi = p_\parallel/p$. Definitions include the Lorentz-gamma γ, electron mass m_e, the velocity v as well as the speed of light c and the parallel direction is placed antiparallel to the main electric field. In a tokamak case this field is parallel to the plasma current time-derivative (usually toroidal). Justified by the fact that small angle collisions dominate in a plasma [19], the collision operator will only be allowed to transfer small momenta. Contrary to the kinetic theory of neutral gases, close encounters do not dominate the behavior in a plasma, but is mainly affected by collective small-angle collisions within the Debye sphere (sphere with radius $r = \lambda_D$) of the particle of interest. Under the assumption that these collectively small collisions dominate, a binary collision operator can be used, since the effects become additive. This assumption corresponds to a large Coulomb logarithm $\ln\Lambda$, where Λ as a fraction, gives the importance of small-angle scatterings over large-angle scatterings. For typical fusion plasmas, it values between 10 and 20. An approximative formula to numerically evaluate $\ln\Lambda$ can be found in e.g. Wesson's book [2]. By the linear superposition above, the Boltzmann collision operator reduces to the Fokker-Planck collision operator. In RE dynamics however, large angle collisions play a special role (avalanche) as well and have to be included using S. This will be addressed in section 2.2. Also a full Boltzmann treatment is possible [20], but is not included in this thesis.

The final equation in our choice of coordinates for the time-evolution of an electron distribution reads

$$\frac{\delta f_e}{\delta t} - eE_\parallel \left(\xi \frac{\delta f_e}{\delta p} + \frac{1-\xi^2}{p} \frac{\delta f_e}{\delta \xi} \right) = \mathrm{C_{FP}}\{f_e\} + \mathrm{S} \tag{2}$$

and is the kinetic equation with a Fokker-Planck collision operator $\mathrm{C_{FP}}\{f_e\}$. Here, $E_\parallel$ is introduced as the magnitude of the parallel electric field. Key to this equation is the collision operator, which describes the small-angle microscopic interactions between particles, and the source term. Section 2.1 will elaborate both these terms.

2.1. Collision operator

As described by Chapman and Cowling, particles, following an inverse-square law of interaction, predominantly undergo small-angle collisions [21]. In a plasma, this inverse-square law is the Coulomb interaction. As its range is infinite, one has to consider the shielding properties of a plasma, limiting the effect of the force to the Debye-length scale and consequently prohibiting the Rutherford cross-section to diverge for small angles [5].

We will take a closer look at the right hand side of eq. (2). First, we investigate the Fokker-Planck collision operator, that is derived from the Boltzmann collision operator and neglect the source term. We will see, that the parallel electron-electron friction force contained in the collision operator is dropping in magnitude for electron velocities above the thermal one. As long as a constant accelerating force stronger than this friction exists, the particle will continuously gain momentum up to relativistic energies. A specific type of electron, the runaway electron is created.

For the Coulomb interaction in question, the main contribution to electron dynamics comes from collisions with other electrons [22] and has the most significant implication. The friction force can be expressed with the slowing down frequency ν_s^{ee} and is featured in the operator as

$$F_C^{ee} = \frac{m_e \langle \Delta v_\parallel \rangle^{ee}}{\Delta t} = -m_e v \nu_s^{ee} \propto G\left(x_e\right). \tag{3}$$

The slowing down frequency of electron-electron collisions indicates the average deceleration due to binary encounters. Angled brackets denote the averaging over all collisions, subscript $\parallel$ dictates the direction to be parallel to the velocity vector of the colliding test particle, $x_e \equiv v_e / v_{th}$ is the velocity (normalized to the thermal velocity $v_{th} = \sqrt{2T_e/m_e}$) and $G\left(x_e\right)$ is the Chandrasekar function

$$G(x) \equiv \frac{\operatorname{erf}(x) - x \cdot \operatorname{erf}'(x)}{2x^2} \rightarrow \begin{cases} \frac{2x}{3\sqrt{\pi}}, x \rightarrow 0 \\ \frac{1}{2x^2}, x \rightarrow \infty \end{cases} \tag{4}$$

$$\operatorname{erf}(x) \equiv \frac{2}{\sqrt{\pi}} \int_0^x e^{-y^2} \mathrm{d}y.$$

Being an important part of the collisional drag force between electrons, the characteristics of the Chandrasekar function (figure 2) will be responsible for the generation of REs. But before that, other effects must be discussed.

Until now, we have only considered elastic electron-electron friction force. Electron-ion collisions in a plasma are also present, but in first approximation can be computed using a simpler operator. For this, it is necessary to assume the ion to be of infinite mass, therefore neglecting energy transfer onto it.

Source term and radiation losses

The source term S in eq. (2) can be understood as a placeholder for various effects on the electron distribution evolution that are not covered by the electric field acceleration term and the collision operator. These include close knock-on collisions, energy losses due to synchrotron radiation and bremsstrahlung, as well as sources and sinks of particles and heat. Knock-on collisions will be treated later (see section 2.2), now the radiation losses will be considered more closely.

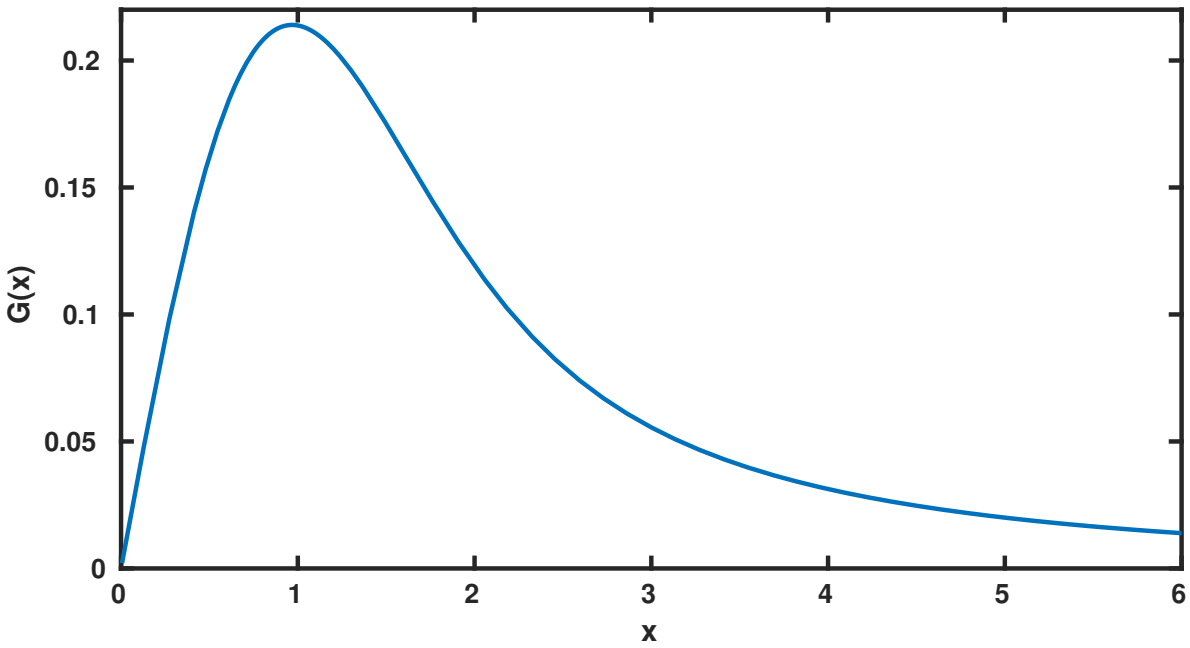

Figure 2: Chandrasekar function $G(x)$.

Synchrotron radiation is the electromagnetic radiation, emitted by charged particles being accelerated perpendicular to their velocity [23]. In a tokamak, it provides a continuous energy loss mechanism for runaway electrons traveling along the torus. The exact emission spectrum is highly sensitive to the shape of the whole distribution [24]. The analytic form of the resulting power spectrum has been derived by I.M. Pankratov [25]. In the same work several approximative formulas are given, which, according to evaluations of Stahl et al. [26] are good approximations to real life applications on tokamaks, depending on the major radius of the device. In the scope of this thesis, the spectrum is not relevant and synchrotron emission will only act as an energy loss mechanism for REs.
Bremsstrahlung is also a radiation reaction-force, which yields in energy losses. In relativistic quantum theory, it can be understood as the emission of a photon due to a binary interaction (inelastic coulomb scattering) of two charged particles. Its magnitude grows with the effective charge $Z_{\text{eff}} = \sum_i n_i Z_i^2 / \sum_i n_i Z_i$ for every ion species i.

2.2. Runaway phenomenon

As mentioned before, the non-monotonic behavior of the collisional friction force F_{C}, characterized by the Chandrasekar function, has an important consequence. Figure 3 (red, dot-dashed) shows the collisional friction force peaking around the thermal velocity v_{th} and then dropping with increasing electron velocity v. Now, if an accelerating force like an electric field acts upon an electron with $v > v_{th}$ and in its magnitude is higher than the counteracting friction, the particle is sped up and increasingly loses less momentum due to collisions than gained from the electric field force. It becomes a "*runaway*",

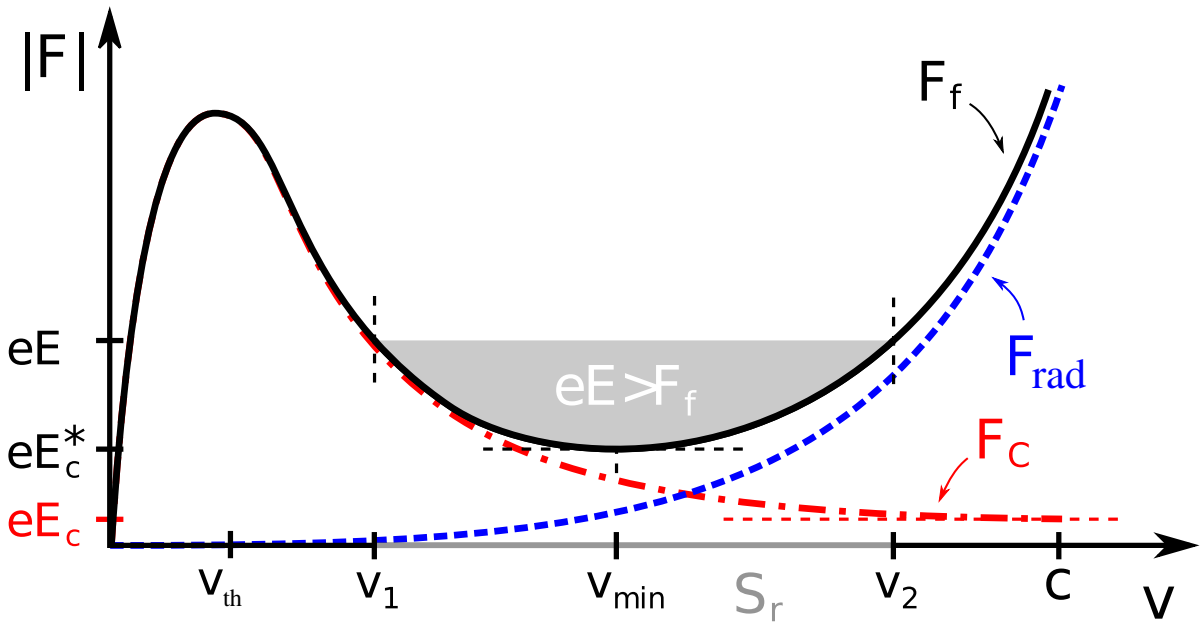

Figure 3: Forces acting on an electron. F_{C} (red, dot-dashed) denotes the collisional electron-electron force, described by eq. (3) and F_{rad} (blue, dashed) the radiation-reaction force. F_{f} is the sum of these two. v_1 and v_2 imped the runaway region S_r. Inclusion of the radiation-reaction force lifts the critical electric field E_C to E_C*. This illustration is a modified one of the original in Stahl's thesis [24].

reaching relativistic velocities. For this reason, F_{C} has an asymptotic minimum value at the speed of light, above which an associated electric field $eE_C = F_{\mathrm{C}}(v \to c)$ can produce runaway electrons. The critical field E_C has been evaluated by Connor and Hastie (1975) [27] to

$$E_C = \frac{m_e c}{e}\nu_{\mathrm{rel}} = \frac{n_e e^3 \ln\Lambda}{4\pi\epsilon_0^2}\frac{1}{m_e c^2}, \tag{5}$$

with the use of the relativistic electron-electron collision frequency [28]

$$\nu_{\mathrm{rel}} = \frac{n_e e^4 \ln\Lambda}{4\pi\epsilon_0^2 m_e^2 c^3}.$$

In plasma physics, the collision frequency is defined by the inverse of the average time t_{ee} it takes for a particle to be deflected by over 90° through an accumulation of small angle collisions. In this picture E_C,is associated with the critical velocity v_c, above which the friction force succumbs the electric field acceleration.

Electric fields in a tokamak are externally applied to drive a plasma current, but are in normal operation mode weaker than the critical value. During a disruption however (section 2.3), an electric field may be induced that is able to drive a significant amount of runaway electrons.

The maximum of the friction force at around $v \approx v_{th}$ is associated with the so called Dreicer field

$$E_D = \frac{n_e e^3 \ln\Lambda}{4\pi\epsilon_0^2} \frac{1}{T_e}, \tag{6}$$

named after H. Dreicer, who historically was the first to research the runaway phenomenon in plasmas [10]. Above the so called *slide-away field* $E_{sa} \simeq 0.214 E_D$ the whole species population eventually becomes a runaway population, an effect known as *slide-away* [29]. Complete slide-away into the runaway regime can occur even at electric fields initially below E_{sa}. Either an increase in temperature lowers the slide-away field over time, or a strong distortion of the bulk is followed by a reduction of friction, leading to a positive feedback loop [30, 31]. Therefore, the most practical electric field regime for runaway research to study is $E_C < E \ll E_{sa}$, since runaways do not exist below the critical value and above the slide-away field (unlikely to be achieved in a disruption) the whole distribution will eventually become one.

Unlike the collisional drag force, the energy losses due to any radiation increase with velocity, as illustrated by the blue, dashed line in figure 3. A momentum conservation law of the radiating electron can be formulated using the radiation-reaction force, where the created photon basically carries momentum away from the particle. It is described via the Abraham-Lorentz-Dirac force [32] and leads to an increase in the slowing-down force an electron experiences, when its velocity approaches the speed of light. A limit on the achievable runaway energy is the consequence. Also, since it is an additional force that is to overcome, the inclusion of the radiation-reaction increases the critical electric field to E_C^*. For $\max|F_f| > eE > F_f = F_{syn} + F_C$ a closed runaway region S_r (grey area) is defined. Apart from that, radiative losses do not significantly impact the RE generation process itself, since it typically takes place at too low velocities.

The friction force of the collision operator mentioned above is just the most significant part of C_{FP}, crucial to the runaway phenomenon. In fact, the Fokker-Planck operator is complex and its treatment often boils down to finding the appropriate approximation for the situation of interest [22]. As I will show in the following section, the possibilities for runaway generation are actually versatile.

Due to the highly energetic nature of REs, electron-positron pair production in a fusion plasma is possible, when the electron collides with a thermal ion. Positrons can also undergo the runaway process [33]. Another runaway process concerns the ions in the plasma. Apart from its theorized appearance in tokamaks, ion runaway has been of interest in astrophysics, where it is believed to explain the abundance of ions in solar flares [34]. In a pure tokamak plasma (full ionization), the two main opposing forces, namely electron-ion friction and electric field acceleration, cancel out completely [35]. In the further work, positron and ion runaway will not be considered.

Runaway generation processes in a tokamak

The specific generation of runaway electrons as they occur in tokamak devices can be grouped into primary and secondary processes. Primary REs provide a seed for secondary production mechanisms to start with. It will become evident, that not only the fraction E/E_C is important for RE generation, but also E/E_D.

Primary generation Most prominently, the primary *Dreicer generation* provides a continuous seed of REs through phase-space diffusion processes. When $E > E_C$ holds, and the velocity-space region above v_c of a distribution has run away, collisions in the bulk, trying to restore the original shape of the distribution, repopulate the tail lost. A steady influx into the runaway region is facilitated. Most notably, the primary Dreicer growth rate depends on $E/E_D \propto T_e$ and not on E/E_C. Handwavingly speaking, the temperature determines the amount of particles being *run-available*.

Secondly, seeds of REs can be generated by hot-tail generation [36, 37, 38] through incomplete thermalization: A plasma, rapidly cooling down, leaves a hot tail in the electron distribution behind, if the cooling down is faster than the high-energy collision time. If an electric field is also present, this drawn-out tail may well be in the runaway region. This process is significant under the circumstance that the collision time scale is significantly lower than the temperature-decay time scale.

Based on our current understanding, both the Dreicer and hot-tail mechanism can be of importance on large tokamaks, depending on the shutdown scenario considered. Hot-tail generation can still be significant if an effort is made to suppress Dreicer generation [11, 39, 40]. Once a seed is present, it can be further multiplied by large-angle collisions, as described in the following.

Secondary generation Once runaways exist (via primary generation), they are able to *knock-on* scatter with thermal electrons from the distribution bulk. These *large-angle* collisions are usually rare in a plasma (by a factor of $\ln\Lambda$ smaller than small-angle collisions) but become important during runaway dynamics. Considering a RE with a momentum at least twice the critical velocity v_c, a close collision may provide enough energy for the thermal electron to enter the runaway region, while the original runaway electron remains in it. The nature of this process enables exponential growth, which is why the process is called *avalanche*. In the original paper by Rosenbluth & Putvinski [41], the approximative solution for a cylindrical plasma in the $E \gg E_C$ limit for $Z = 1$, the growth rate can be evaluated to

$$\frac{\mathrm{d}n_{RE,ava}}{\mathrm{d}t} \propto n_{RE,ava}\left(\frac{E}{E_C} - 1\right). \tag{7}$$

Contrary to the primary generation, here the (linear) E/E_C-dependence is vivid. I will provide a more detailed description of secondary generation in section 3.1.3.

2.3. Disruptions

In the context of tokamaks, a disruption is a sudden loss of plasma confinement. Figure 4 shows the measurements of such a disruptive case, as occurred in shot #33108 in the ASDEX Upgrade tokamak (AUG) [17] and will serve as template to go through the physical process. A technique used in AUG to mitigate or trigger (in this shot trigger) disruptions in a controlled manner is by massive gas injection (MGI).

The collapse of confinement leads to the plasma cooling down, be it due to e.g. physical contact with the surrounding vessel or due to an increase in losses. Subsequently, the core temperature T_e drops significantly (figure 4a). The magnetohydrodynamic (MHD) energy W_{MHD} contained is radiated away, amplified by an impure plasma composition should the unconfined plasma touch the wall or, in that very event, even conducted away through physical contact. The MGI-systems are triggered at t_{MGI} and consequently give rise to the increasing density n_e (figure 4b). The area contoured magenta marks this phase called *thermal quench* (TQ). Loss of temperature during the TQ leads to a gradual reversal of the excellent conductive properties of the plasma, as the resistivity rises with $\eta \propto T_e^{-3/2}$, introducing the *current quench* (CQ) phase shaded green in the depictions. Figure 4c shows the plasma current I_p consequently collapsing and inducing an internal electric field E_{tor} in toroidal direction. This electric field generates REs as indicated by the hard X-ray measurements (figure 4d). Runaway electrons emit X-rays through bremsstrahlung processes in either the plasma, or when the REs hit plasma-facing components. These runaway electrons carry a significant amount of the original plasma current, preventing it from collapsing completely and saturating at about 0.2 MA. Roughly 25% of the original plasma current have been converted into runaway current.

Apart from the initial threats to the mechanical device, like the danger from heat loads onto any plasma-facing component and the mechanical stresses caused by induced currents and the collapsing I_p and B, the runaway beam poses a great peril to future tokamaks. Currently, JET (Joint European Torus) in Culham, UK is the biggest tokamak device ($R = 2.9$ m) available, capable of carrying a plasma current of $I_p = 4.0$ MA. During a disruption, up to more than half the initial current can be converted into runaway current [42], leaving high amounts of energy the plasma-facing components have to bear. In the present, the devices available are mostly able to withstand the threat. But in order to accomplish a net fusion power gain, the devices have to get bigger, containing more energy.

The next big project, ITER [43], is to be built with a major radius of $R = 6.2$ m, carrying an expected plasma current of 15 MA. The number of runaways generated via avalanche (see section 2.2) is predicted to scale exponentially with the plasma current [6], and is therefore crucial to research. Predictive understanding of the theory behind RE mitigation and control is required for the success of ITER, as ad-hoc, empirical tuning is not a desirable option.

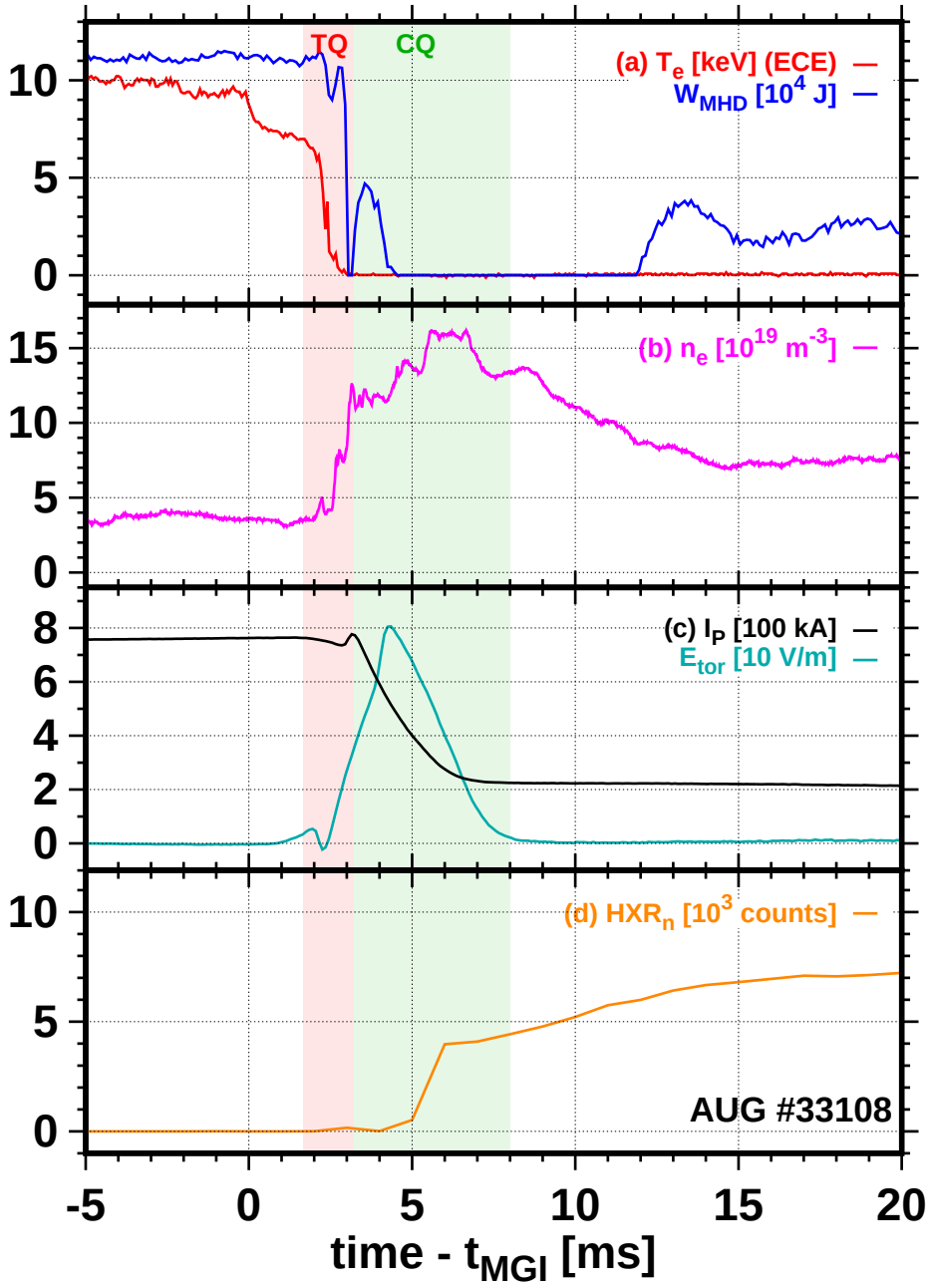

Figure 4: Experimental signals of key quantities during a disruption in the AUG shot #33108, shown over the timescale gauged to the instant of time t_{MGI}, when the massive gas injection is triggered. Graph (a) shows the core electron temperature T_e obtained from the electron cyclotron emission (ECE) and the reconstructed magnetohydrodynamic (MHD) energy W_{MHD}. The ECE temperature measurement cuts off above a density of $n_e = 1.94{\cdot}10^{19} \cdot B^2$ [T]. (b) Core electron density n_e measured by the CO_2 interferometer system, (c) plasma current I_p & calculated core toroidal electric field E_{tor}, and (d) the hard X-ray count HXR_n. TQ and CQ mark the areas identified as *thermal quench* and *current quench*.

3. Simulation of an electron distribution in momentum-space

In this chapter, I introduce a numerical Fokker-Planck solver. Analytical solutions to the kinetic equations only exist in limited cases, e.g. for avalanche dominated cases [44]. This circumstance requires numerical solutions. For this purpose, several tools exist, varying in their capabilities and strengths through their different assumptions and simplifications. This thesis is build around one of these tools, introduced in the following.

3.1. CODE

"CODE" (COllisional Distribution of Electrons) is a MATLAB written numerical tool, designed to solve the kinetic equation with a *linearized* Fokker-Planck collision operator for electrons (eq. (2)), first introduced by Landreman, Stahl and Fülöp [45]. Being zero-dimensional in space and using linearized operators, CODE does not include spatial features, nor does it allow distributions to deviate far from a Maxwellian (the *number* of runaway electrons has to be small - few % - compared to the bulk). Its strength lies in its fast run times, lasting from minutes to days on a single computer. This especially shows in the time-independent mode, where a long-time (quasi-)equilibrium distribution function f_e of the Fokker-Planck equation (2) is determined ($\delta f_e/\delta t = 0$, steady state). The numerical implementation is based on a finite-difference discretized nonmonotonic grid in momentum space p and a spectral Legendre-mode decomposition in ξ. This implementation has been chosen due to the fact, that the collision operator is the main origin of complexity and is best described by its Eigenfunctions, which are the Legendre-polynomials. For time-advance, an implicit time-stepping scheme is implemented. At reasonable grid sizes and constant time-parameters, CODE can efficiently be run on a desktop computer, since the whole system is hereby embodied by just one large sparse matrix, typically sized in orders of thousand to millions of entries.

We describe the collision operator $\mathrm{C_{FP}}\{f_e\}$ as a function of pitch and momentum and introduce the normalization $F = (\pi^{3/2} m_e^3 v_{th}^3/n_e) f_e$, so that $F \to 1$ for $y \to 0$. The kinetic equation forms thereupon into a linear inhomogeneous partial differential equation in 2D

$$\frac{\delta F}{\delta t} + MF = S \tag{8}$$

where M is a linear, time-independent (for constant plasma parameters) differential matrix operator and F is discretized using the Legendre polynomials $P_L(\xi)$

$$F(y,\xi) = \sum_{L=0}^{\infty} F_L(y) P_L(\xi)$$

The full equation written out can be found in the appendix (eq.(26)) as well as the discretized version of it (eq. (27)), which shall later be investigated for a special benchmark

case (section 3.2.4). CODE has been improved and constantly developed since its initial paper on it was launched in December 2013. Described in a follow-up paper [46] is the addition of features such as time-dependent plasma parameters, a field-particle term for the collision operator (see section 3.1.1) as well as improved avalanche operators (see section 3.1.3). Features like the synchrotron radiation operator [47] and bremsstrahlungs radiation reaction [48] were implemented later.

Physical input parameters are temperature T, electron-density n_e, effective ion charge Z_{eff}, external electric E and magnetic field B, all of which, with the exception of B can be time-dependent. The temperature is a necessity to define the Maxwellian

$$f_M = \frac{n_e}{\pi^{3/2} v_{th}^3} \exp\left(-\frac{v}{v_{\text{th}}}\right). \tag{9}$$

It describes the electron-population bulk in momentum space and is often a starting point for the calculation, even though an arbitrary initial distribution can be set to evolve via CODE. Even though CODE solves for the entire distribution (full-f), it is a linearized tool. As will be shown in the follow-up section, the collision operator is linearized around a Maxwellian, meaning that the particles collide with a Maxwellian described by n_e and T. Non-linear tools have been developed recently (for instance NORSE [30]), but are out of the scope of this thesis.

Unlike the density and temperature, the effective ion charge, the electric and magnetic field can be set to zero. Hereby individual physical effects can be segregated, e.g. $B = 0$ corresponds to a situation without synchrotron losses, $Z = 0$ is eliminating electron-ion collisions, while $E = 0$ can be used to take a look into rethermalization processes. Same goes for bremsstrahlung and avalanche-operators, which can both be turned off. The electric field normalization is such, that electrons are accelerated towards positive parallel momentum

$$\hat{E} = \frac{-eE}{m_e v_{th} \nu_{ee}}$$

with the Braginskii electron collision frequency [28]

$$\nu_{ee} = \frac{4\sqrt{2\pi} e^4 n_e \ln\Lambda}{3\sqrt{m_e} T^{3/2}}.$$

Main numerical parameters include N_ξ, which gives the number of Legendre-Polynomials, N_y, which sets the number of points on the discretized momentum-grid and $y_{\max}$, being the maximum extent on the parallel grid axis. The spacing of the grid can be non-monotonic, giving a high resolution for the densely populated low-energy bulk and diluting for the high-energy tail, where the distribution function varies only on large scales. The resulting size of the matrix M is roughly given by $N_y \times N_\xi$. The discretization parameters can be extended automatically by CODE itself, once the distribution at the end of the grid rises above a certain threshold. For long-term runs with growing

energy-tails this can save a lot of calculation time during the early stages of the evolution[49].

In time-dependent mode, the number of parameters extend by two, where $t_{\max}$ is the calculation time and dt is the time-stepping. dt is mainly determined by the speed of the evolution of the distribution and should be set such, that abrupt changes in f_e cannot induce numerical errors. CODE advances the calculation using backward Euler method and will advance in time using a single matrix inversion.

Once a time-dependent temperature is chosen, CODE features reference normalization to improve the run-time. Hereby the grid $y = \gamma v/v_{th}$ and the reference Maxwellian (eq.(9) are normalized to the constant reference temperature (and density) grid $T_{ref} = \bar{T}$ and $n_{ref} = \bar{n}$. This means that the grid does not need to be rebuild in each and every step dt. For large variations of the temperature it is recommended to frequently adjust the reference density and temperature. The time-stepping can also be chosen as a function of instantaneous reference collision times.

3.1.1. Collision operator

In CODE, the ion-species is approximated as being a stationary Maxwellian for particles of infinite mass. This greatly simplifies the electron-ion collision operator in first approximation, to be only dependent on Z_{eff} [22]. In pursuit of describing electrons colliding, we introduce a small perturbation f_1 to the Maxwellian $f_M = f - f_1$, enabling to write the Fokker-Planck electron-electron collision operator in its linearized form [46],

$$\mathrm{C_{ee}}\{f\} \simeq \mathrm{C^{l}_{ee}}\{f\} = \mathrm{C^{tp}_{ee}} + \mathrm{C^{fp}_{ee}}, \tag{10}$$

where *tp* and *fp* respectively denote the *test-particle* and the *field-particle* terms and can be classified as follows: (a) the test-particle term $\mathrm{C^{tp}}\{f_1, f_M\}$ represents the perturbation f_1 colliding with the bulk f_M and (b) the field-particle term $\mathrm{C^{fp}}\{f_M, f_1\}$ shows the reaction of the bulk to this very perturbation. Both terms are therefore of 1st order in f_1, while the 2nd order $\mathrm{C}\{f_1, f_1\}$ is neglected in the linearzation. 0th order cancels out as the collision operator vanishes for a Maxwellian. Introduced in Papp et al. [50], the original collision operator implemented in CODE was a relativistic test-particle term $\mathrm{C^{tp}}$ valid for arbitrary energies

$$\mathrm{C^{tp}_{ee}} = \frac{3\sqrt{\pi}\bar{\nu}_{ee}}{4}\bar{v}_{th}^3 y^{-2}\left(\frac{\partial}{\partial y}\left[y^2\Psi\left(\frac{1}{x}\frac{\partial}{\partial y} + \frac{2}{\bar{v}_{th}^2}\right)F\right] + \frac{c_\xi}{2x}\frac{\partial}{\partial \xi}(1-\xi^2)\frac{\partial F}{\partial \xi}\right), \tag{11}$$

where the bars denote a quantity to be normalized to its reference value (for reasons mentioned in section 3.1). Furthermore, the quantity $c_\xi = Z + \Phi - \Psi + \bar{v}_e^2\delta^4 x^2/2$ is being used with $\Phi = \Phi(x/\bar{v}_e)$ and $\Psi = \Psi(x/\bar{v}_e) = \bar{v}_e^2\left[\Phi - \bar{v}_e^{-1} x\, d\Phi/d(x/\bar{v}_e)\right]/2x^2$, which respectively are the Error and Chandrasekhar functions, including the normalized speed $x = y/\gamma = v/\bar{v}_{th}$ and $\delta = \bar{v}_{th}/c$. Hereby the assumption of a small δ is being made, correctly representing a non-relativistic thermal population only. The (11) test particle

operator however was developed for test particle studies. Therefore it does not conserve momentum or energy, just the number of particles. Meaning that a sudden loss of electric field strength is abruptly followed by a relaxation of the distribution function to its Maxwellian, if only this test-particle operator is considered.

The conservation of energy and momentum can be restored by adding the non-relativistic field-particle term

$$\mathrm{C}_{\mathrm{ee}}^{\mathrm{fp}} = \frac{3\bar{\nu}_{ee}}{4\pi} e^{-\bar{v}_2^{-2}x^2} \left[\frac{2x^2}{\bar{v}_e^4} \frac{\partial^2 G}{\partial x^2} - \frac{2}{\bar{v}_e^2} H + 4\pi F \right], \tag{12}$$

using the Rosenbluth potentials of the distribution

$$\bar{v}_e^2 \nabla_v^2 H = -4\pi F, \quad \bar{v}_e^2 \nabla_v^2 G = 2H.$$

Its limit of validity lies in the non-relativistic assumption of the field-particle term. In Figure 5 I show, how the relativistic collision operator $\mathrm{C}_{\mathrm{rel}}^{\mathrm{tp}}$, which solely contains the test-particle term, does not reproduce the Spitzer conductivity [51]

$$\sigma_{\mathrm{SP}} \simeq 2 \frac{n_e e^2}{Z_{\mathrm{eff}} m_e \nu_{ee}} = \frac{3}{2\sqrt{2\pi m_e} e^2} \frac{T^{3/2}}{Z_{\mathrm{eff}} \ln\Lambda}, \tag{13}$$

but only roughly half its value (as predicted by Helander and Sigmar [22]). The field-particle term is crucial for the conductivity $\sigma = j/E$, for it is responsible for the bulk's characteristics. The property to "conduct" can in the end be understood as the current-response of the distribution to an electric field E. This meaning of conductivity increasingly fades with growing E/E_D, as a rising number of runaway electrons produced contribute to the current itself (see section 5.4).

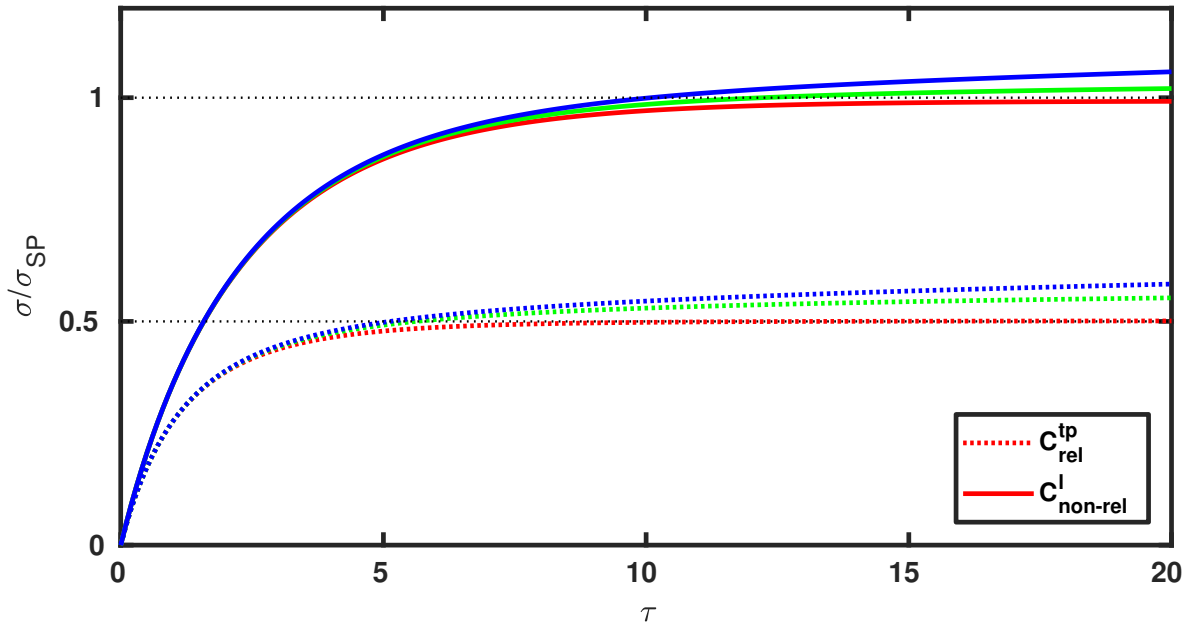

Figure 5: Conductivity, normalized to the Spitzer value σ_{SP} for two different collision operators (see section 3.1.1) over time given in collision times (red: $E/E_D = 1\%$, green: $E/E_D = 5\%$, blue: $E/E_D = 6\%$). The conductivity $\sigma = j/E$ is evaluated using the current j, which is taken from the first moment of the distribution. Parameters are $T = 1$ keV, $n = 2{\cdot}10^{19}$ m^{-3} and $Z = 1$, and no avalanche generation has been used for reasons of simplicity.

The non-relativity of the field-particle term can be justified, since the bulk is not relativistic in tokamak flat-tops and post-disruptive plasmas. For the simulations of this thesis, I will use the fully conservative collision operator, when self-consistent treatment of the electric field is necessary.

3.1.2. Operators for radiation losses

The synchrotron loss operator for the radiation reaction force originates from the Abraham-Lorentz-Dirac force acting on an electron [32]. Under the assumption that the particle is accelerated predominantly perpendicular to its velocity (dominant magnetic forces), the expression yields [24]

$$F^p_{\text{syn}} = -\frac{\gamma p(1-\xi^2)}{\tau_r}, \quad F^\xi_{\text{syn}} = -\frac{p\xi\sqrt{1-\xi^2}}{\gamma\tau_r}. \tag{14}$$

Herby $\tau_r = 6\pi\epsilon_0(m_e c)^3/e^4B^2$ is the radiation-damping timescale. As evident from the expression, the force vanishes for parallel and antiparallel movement ($\xi = \pm 1$) and is proportional to B^2.

In CODE, bremsstrahlung is included in two different ways, the first one being a simple average mean force [52]

$$\frac{\mathrm{d}p_{\parallel}}{\mathrm{d}t} = F_B = \frac{4}{137} m_e c^2 r_e^2 n_e (Z_{\mathrm{eff}} + 1)\gamma \left(\log 2\gamma - \frac{1}{3} \right), \tag{15}$$

where r_e is the classical electron radius. Note that, while the synchrotron radiation is proportional to the square of both the magnetic field strength B and the major radius R [53], bremsstrahlung is independent of those.

The second description is a kinetic one, where the radiation emission is modeled as a binary collision between two charged particles, spontaneously creating a photon as a result [48]. Absorption of already existing photons and stimulated bremsstrahlung emissions are neglected, as their impact is calculated to only be important for dense, or large plasmas, barely affecting electron runaway distributions in tokamak disruption scenarios [54]. The main feature of the kinetic description is taking the energy distribution of the emitted photons into account. The calculations lead to the somewhat counter-intuitive result, that low-energy photons can significantly contribute to large angular deflection of the electrons. The mean force model however uses a high-energy limit of photons for the cross-section, forming a rather sharply peaked distribution function, unlike the Boltzmann-model, where the large-angle deflections cause the population to extend further in perpendicular momentum. The Boltzmann-model bremsstrahlung operator therefore synergizes with the synchrotron operator due to the $p_{\perp}^2$-proportionality of the latter.

In this thesis I will use the (15) pitch-independent one, since mainly integral quantities will be of interest.

3.1.3. Operators for large angle collisions (avalanche)

Since large angle collisions cannot be captured by the Fokker-Planck formalism, close Coulomb scattering is implemented in CODE via the source term $\hat{\mathrm{S}}$ to the kinetic equation (2). Of this, there are two different source-operators (Rosenbluth-Putvinski [41] and Chiu [55]).
The Rosenbluth-Putvinski operator in the momentum space coordinate (y, ξ) for an electron with the relativistic mass factor γ was derived as [41]

$$\hat{\mathrm{S}}_{\mathrm{RP}}(y,\xi) = \frac{n_{RE}}{n} \bar{n}^2 \left(\frac{3\pi\delta^3}{16 \ln\bar{\Lambda}} \delta_D(\xi - \xi_2) \frac{1}{y^2} \frac{\partial}{\partial y} \frac{1}{1 - \sqrt{1 + \delta^2 y^2}} \right), \tag{16}$$

inherently carrying the important property of proportionality to the runaway electron number density n_{RE} and using the Dirac δ_D-function to assume the creation of secondary particles to only take place on the curve $\xi = \xi_2 = \delta y / (1 + \sqrt{1 + \delta^2 y^2})$. Latter originates from the simplifying assumption that the momentum of all the incoming particles is infinite ($p = \gamma v / c = \delta y \gg 1$) and its pitch-angle equal zero ($\xi = 1$). This source-operator

however, does not take the energy distribution of the runaway electrons into account, making it possible to create electrons with an energy higher than any of the electrons available. Another issue arises during the discretization of ξ into Legendre-modes, since the Dirac δ_D-function succumbs to the Gibbs phenomenon, creating oscillations in pitch [46].
A more advanced operator for close-angle scattering in CODE is a source-operator given by Chiu et al. [55]

$$\hat{\mathrm{S}}_{\mathrm{Ch}}(y,\xi) = \bar{n}\frac{2\pi e^4}{m_2^2c^3}\frac{n\delta^3}{\nu_{ee}}y_{in}^4\tilde{f}(p_{in})\Sigma(\gamma,\gamma_{in}), \tag{17}$$

where the Møller scattering cross section

$$\Sigma(\gamma,\gamma_{in}) = \frac{\gamma_{in}^2}{(\gamma_{in}^2-1)(\gamma-1)^2(\gamma_{in}-\gamma)^2}* \\ \left[(\gamma_{in}-1)^2 - \frac{(\gamma-1)(\gamma_{in}-\gamma)}{\gamma_{in}^2}\left(2\gamma_{in}^2+2\gamma_{in}-1-(\gamma-1)(\gamma_{in}-\gamma)\right)\right]$$

is multiplied with the pitch-angle-averaged distribution $\tilde{f}$ of incoming runaways with relativistic mass factor γ_{in} and momentum p_{in}, therefore includes the energy distribution of the incoming particles. This avalanche-operator has been advanced by a full Boltzmann-treatment by Embréus [56], taking full pitch-dependence into account.

Both operators are compared to each other in figure 6. The (a) Rosenbluth-Putvinski operator is non-vanishing only along the trajectory ξ_2 and creates numerical noise due to the Gibbs phenomenon. The (b) Chiu operator takes the energy distribution of the incoming particle into account by restricting the source operator to the region

$$\xi_{min} \leq \xi \leq \xi_{\max}$$

with

$$\xi_{min} = \sqrt{\frac{(\gamma-1)(\gamma_{\max}+1)}{(\gamma+1)(\gamma_{\max}-1)}}, \quad \xi = \sqrt{\frac{(\gamma-1)(\gamma_{in}+1)}{(\gamma+1)(\gamma_{in}-1)}}, \quad \xi_{\max} = \sqrt{\frac{\gamma}{\gamma+1}}.$$

In order to prevent double-counting of small and large angle collisions, both operators are restricted to a high-energy regime, where small-angle collisions fade in importance. This cut-off boundary is usually chosen as the critical momentum trajectory y_s, but can also be changed. Considering the fact that the source magnitude grows for decreasing momenta, lowering the cut-off boundary has to be done with care. The standard choice of the cut-off boundary to be the critical momentum y_c is reinforced by calculations of Nilsson et al. [57]. These state (shown for the Rosenbluth-Potvinski operator), that even if a secondary generated particle is placed on the momentum scale at $y_{th} < y < y_c$, it is most likely to be slowed down into the bulk again. The other option would be the diffusion of this very particle into the runaway region, thereby artificially increasing the Dreicer flux based solely on the choice of the cut-off momentum $y_{\mathrm{cut-off}}$. Since

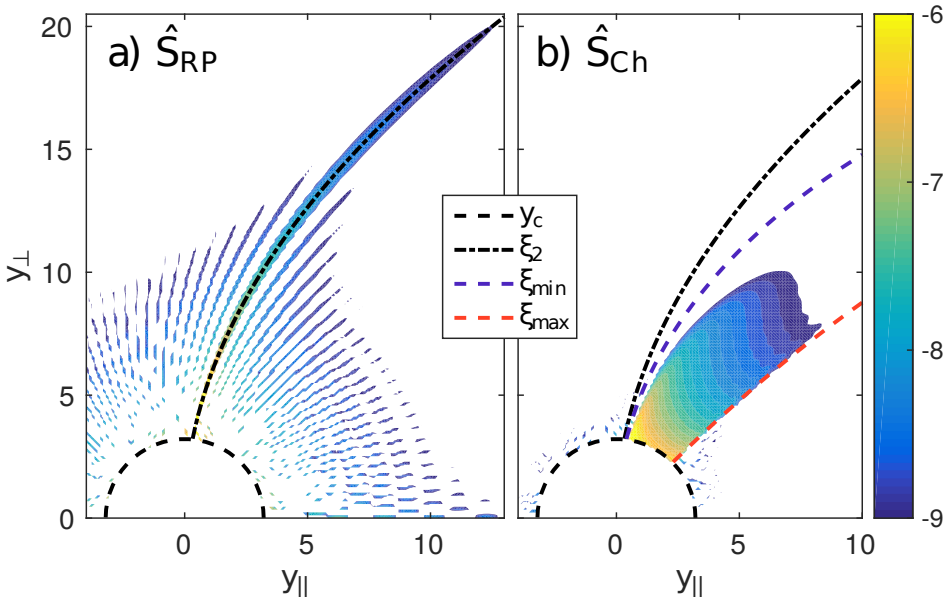

Figure 6: Contour plots of the source magnitudes $\log_{10}\hat{S}$ of (a) eq.(16) and (b) eq.(17) in momentum space of the same electron distribution. y_c is the critical momentum, below which the source magnitudes are zero to prevent double counting with small-angle collisions. Parameters are $T = 1$ keV, $n = 5{\cdot}10^{19}$ m^{-3}, $Z_{\text{eff}} = 1$, $E = 1$ V/m, $t_{\max} = 300$ $[1/\nu_{ee}]$ and $y_{\max} = 70$. This illustration is taken from the "CODE improvements paper" [46].

the avalanche multiplication factor γ_A is shown to fulfill $\gamma_A(y_{\text{cut-off}})/\gamma_A(y_c) \to 0$ for $y_{\text{cut-off}} \to y_c$, the cut-off momentum is best chosen to be the critical momentum.

The source magnitude of the Rosenbluth-Putvinski operator can also be driven by "fast particles" rather than runaways. Fast particles are defined as particles above a certain momentum threshold or as part of the distribution, where the deviation from the Maxwellian is above a threshold $f_e/f_M >$ const.. Investigation of scenarios, where $E < E_C$ occurs (e.g. during post-disruption runaway decay in low inductance tokamaks) is therefore made possible, but also becomes sensitive to the definition of "fast particles". But unless otherwise stated, the Rosenbluth-Putvisnki operator will be driven by runaways.

3.2. Basic physical validation

3.2.1. Runaway process

A runaway electron distribution in its simplest form is described as a population of electrons beyond some velocity v_c (see figure 3), above which an electric field $E > E_c$ always surmounts the friction force. Since the velocities these electrons can reach are a significant portion of the speed of light, it is more practical to talk in terms of normalized momentum $p = \gamma v/c$. The second coordinate of our system to solve (eq. (2)), is the

cosine of the pitch angle $\xi = p_\parallel/p$, making it customary to illustrate the results by means of $p_\parallel$ and $p_\perp$. Due to symmetry, only positive values of perpendicular momentum will be plotted. The preferential direction of the electric field introduces a pitch-dependence to the critical momentum $p_c = \gamma_c v_c/c$ [58]. In order to define the separatrix, i.e. this pitch-dependent momentum trajectory p_s in phase-space that separates the bulk from the runaway region, CODE demands force-balance between electric field F_E^i, collisional electron friction F_C^i and synchrotron radiation-reaction F_{Syn}^i for each coordinate $i \in \{p, \xi\}$ [24]. It holds $p_s \to p_c$ for $\xi \to 1$ (positive parallel axis).

The shape, magnitude and dynamic of a distribution function reveals a lot of the procedure forming it. I will use this in order to explain the runaway process in its most general kind. Figure 7 shows the time-evolution of an initially isotropic distribution, under the influence of an electric field (figure 7a), seconded by a stepwise growing magnetic field (figure 7(b-c)). By comparison, figure 7(d-e) illustrates, how the distribution would have evolved without synchrotron losses ($B = 0$).

At first, only electric field acceleration and collisions are present in the system (figure 7a). The constant electric force drags particles from the main bulk parallel to the axis in positive direction. At this point, only collisional friction is counteracting this motion and can therefore be increased by a larger electron density. After only $t = 200\ [1/\nu_{ee}] = 0.01$ s, the average energies have grown substantially

$$\frac{E_{av,bulk}(t=200)\ [\mathrm{keV}]}{E_{av,bulk}(t=0)\ [\mathrm{keV}]} = \frac{6.1}{4.5}, \quad \frac{E_{av,RE}(t=200)\ [\mathrm{keV}]}{E_{av,RE}(t=0)\ [\mathrm{keV}]} = \frac{180}{36},$$

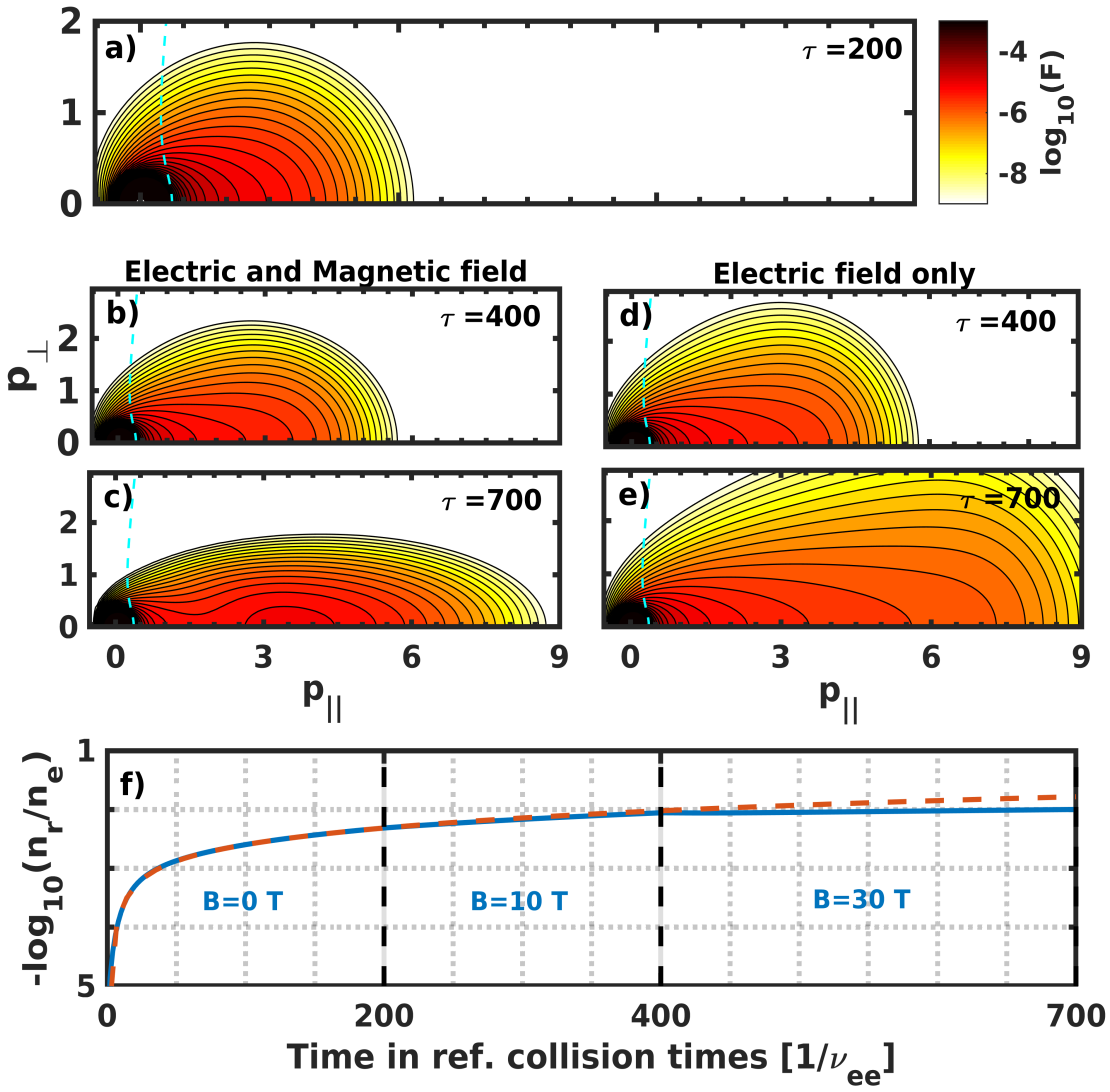

Figure 7: An electron distribution under the influence of an electric field (a-e). Plots (b-c) show how the distribution in plot (a) evolves being supported by a magnetic field in comparison to the electric field only case (d-e). Magnitudes of the magnetic field at given times can be found in plot (f) and are chosen extreme for ease of illustration. Indicated with a cyan, dashed line is the pitch-dependent critical momentum $p_s(\xi)$, which defines the runaway region. The axes show perpendicular and parallel normalized momentum $p = \gamma v/c$ at a certain number of collision times $\tau = 6.9 \times 10^{-5}$ s of the electrons. Plot (f) compares the runaway fraction n_r/n_e of (b-c) (blue, continuous) and (d-e) (orange, dashed). Input parameters are $T = 3000$ eV, $n_e = 5{\cdot}10^{19}$ m^{-3}, $Z = 1$, and $E = 0.35$ [V/m] or $E/E_c = 8.4$. Calculated using the relativistic test particle collision operator, and no avalanche source.

mainly contributing to the runaway region itself. The distribution is also extending in perpendicular direction, due to energy transfer from pitch-angle scattering. As seen in figure 7f, a runaway fraction of around 1% is quickly reached. At this point in time, a strong magnetic field is set, allowing synchrotron losses to take part in influencing the shape. In a simplified single particle picture, the total emitted synchrotron power of a electron gyrating in a homogeneous magnetized plasma scales with [24]

$$P_{tot} \propto B^2 p_\perp^2,$$

leading to energy losses in perpendicular direction. The effect becomes apparent when comparing the results to the distributions, which evolved without magnetic field. The runaway fractions of both cases are shown in figure 7f. Synchrotron losses do not directly affect the runaway growth rate in a significant way, but when using the pitch-dependent definition of the runaway region, an exaggerated magnetic field is capable of "removing" particles from the runaway region, because the separatrix is not a vertical line at p_c but a trajectory (figure 7, cyan, dashed lines). They also change the maximum energy runaways can reach, and change the shape of the distribution, which is influential when considering other physical effects.

3.2.2. Convergence scans

The choice of numerical parameters is a balance act of necessary precision and computation time. For long lasting simulations to work properly, a feeling for parameters to set has to be established beforehand. For N_ξ and N_y figure 8 shows two convergence scans in a steady state calculation of CODE. Assuming the blue lines to be a converged solution ($N_\xi = 25$, $N_y = 150$), the resulting matrix size is 3726 and the time to assemble and solve the system is respectively ~ 0.03 s. This proportion of N_ξ to N_y is a good a rule of thumb.

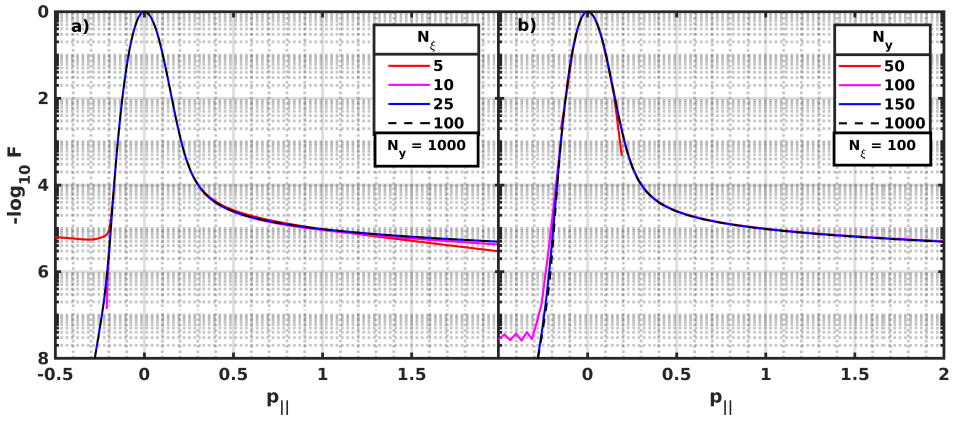

Figure 8: Convergence of distributions in (a) N_ξ and (b) N_y for a CODE steady state calculation. Input parameters are: $T = 1000$ eV, $B = 3$ T, $n_e = 10^{19}$ m^{-3}, $Z = 1$ and $E = 0.2$ V/m. Blue and black lines overlay completely. Lines abruptly ending indicate insufficient numerical parameters creating negative values in the distribution, which are ignored in the logarithmic plot.

Complexity is added though time-dependency, bremsstrahlung and large-angle collision operators. Matrix sizes increase to millions of entries for high energy problems, and elevate the computation time up to several days for advanced real-life applications. Once the calculation is independent of the grid, the time-step dt in time-advance mode has to be sufficient enough as well. In time-advance mode, CODE has the ability to adjust its own resolution parameters to a certain degree.

3.2.3. Time-evolution and rethermalization

Figure 9a depicts a time-evolving simulation of a distribution together with the steady state solution for the same physical parameters, showing excellent convergence. The negative parallel momentum-space is magnified in figure 9b. The deviation from $\tau = 0$, which is the starting Maxwellian, indicates particles to be scattered faster in angle than they scatter in energy, meaning the thermalization is succumbed to small-angle Coulomb-scattering. Some particles "turn around" faster than they can thermalize to the initial distribution during evolution, giving rise to this backwards tail. Figure 9c shows how the electron population then returns to its Maxwellian form after the electric field strength is set to zero. The timescale of the process affirms the previous observation, that the cumulative effect of many small angle scatterings qualitatively dominate the thermalization.

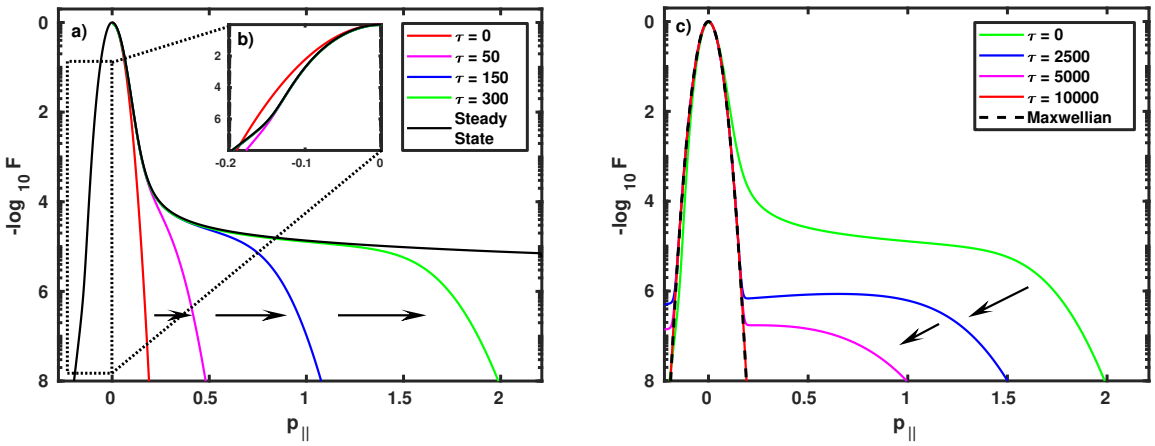

Figure 9: **a**): Convergence of the parallel distribution function over time to the steady state solution. **b**): A closer look at the negative tail. **c**): Rethermalization after turning the electric field off. Time τ is given in units of electron collision frequency $\nu_{ee} = 7.8 \times 10^4$ s^{-1} and the y-axis shows the distribution function normalized according to $F = (\sqrt{\pi} m v_{th})^3 \, n_e^{-1} f$. The arrows indicate the direction of the time-evolution. Input parameters are: $T = 500$ eV, $B = 2$ T, $n_e = 2{\cdot}10^{19}$ m^{-3}, $Z = 1$ and $E = 0.8$ V/m

3.2.4. Validation with previously published data

Classical results, such as the ones calculated by Kulsrud et al. [59] are met by CODE in figure 10. The calculations are non-relativistic (Dreicer generation occurs close to the thermal bulk, $\gamma_c \simeq 1$) and do not include close-angle collisions, wherefore

$$\delta \to 0, \quad x \equiv \frac{v}{v_e} = \frac{y}{\sqrt{1+\delta^2 y^2}} \to y$$

holds. With the assumptions above, the discretized kinetic formula (appendix, eq. (27)) reduces for the zeroth Legendre-Mode $L = 0$ to

$$\frac{\partial F_0}{\partial \hat{t}} + \frac{\hat{E}}{3}\frac{\partial}{\partial y} F_1 - \frac{3\sqrt{\pi}}{4}\left(\frac{\Psi(y)}{y}\frac{\partial^2}{\partial y^2} + \frac{2\Psi(y)}{y} + \frac{d\Psi(y)}{dy} + \frac{\phi(y)-\Psi(y)}{y^2}\frac{\partial}{\partial y}\right) F_0 = \hat{S}_0.$$

Now the operation $4\pi^{-1/2}\int_{y_b}^{\infty} y^2 \, dy$ is applied for some boundary value y_b, above which the source is assumed to be negligible. Defining the number of runaway electrons n_{RE} as particles in velocity space above this boundary value $y > y_b$ gives $n_{RE} = 2\pi \int_{m_e v_e y_b}^{\infty} p^2 \, dp \int_{-1}^{-1} f \, d\xi$ and finally yields the runaway growth rate

$$\gamma_{RE} \equiv \frac{1}{n_e \nu_{ee}}\frac{dn_{RE}}{dt} = \underbrace{-\frac{4}{\sqrt{\pi}}\frac{\hat{E}}{3} y_b^2 F_1(y_b)}_{\text{electromagnetic part}} + \underbrace{3\left(\Psi(y_b) y_b \frac{\partial}{\partial y} + 2\Psi(y_b) y_b^2\right) F_0(y_b)}_{\text{collisional part}}. \qquad (18)$$

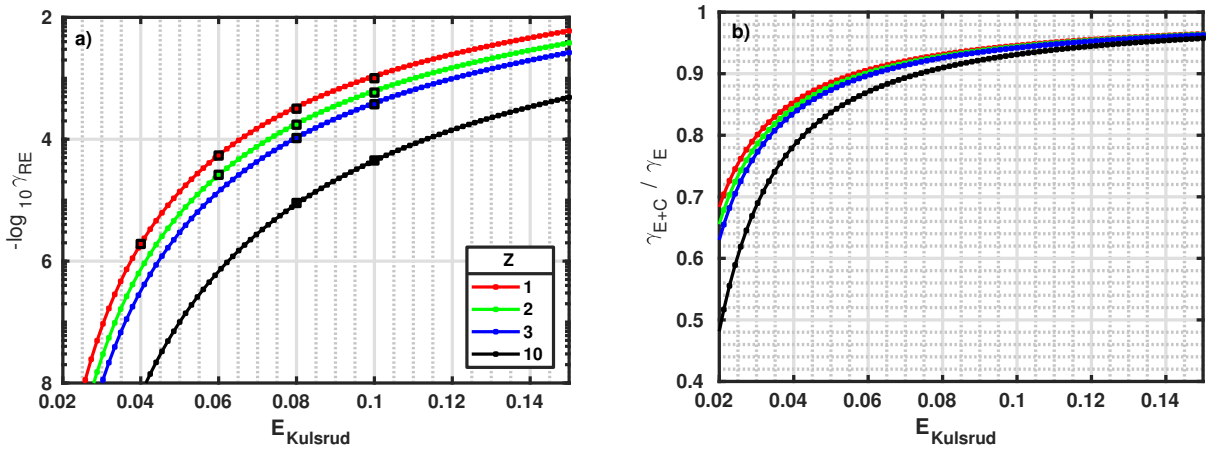

Figure 10: (a) Benchmarking the runaway growth rate of CODE against results obtained by Kulsrud et al. [59] in the non-relativistic limit. As in the paper that is being compared to, $y_b = 10$ has been used. Markers correspond to the Kulsrud values. Excellent agreement is archived. (b) shows the vanishing importance of the collisional influence on the growth rate in this regime. Subscript E stands for the *electromagnetic part* and C for the *collisional part* in eq.(18).

To obtain this result, it has to be assumed, that for $y_b < y \to \infty$, the Legendre mode F_1, as well as the collisional diffusion in velocity space vanishes, corresponding to $(\phi(y_b) - \Psi(y_b)) \to 0$. For reasonably high y_b this can justifiably be done. From eq. (18) the runaway growth rate in the non-relativistic limit can therefore be computed from the zeroth and first Legendre mode. F_0, responsible for the collisional part, is hereby even reasonably negligible as shown in figure 10b. The electric field defined in the original paper by Kulsrud is given by

$$E_{\text{Kulsrud}} = \frac{2}{3\sqrt{\pi}}\hat{E} = \frac{2eE}{3\sqrt{\pi}m_e v_{th}\nu_{ee}}$$

Slightly changing the normalization (Kulsrud defined thermal velocity as $v_{th} = \sqrt{T/m}$ without the factor 2) eventually makes the Kulsrud growth rates comparable with CODE methods

$$\gamma_{RE} = -\frac{4\sqrt{2}}{9\pi}\hat{E}y_b^2 F_1(y_b) + \frac{9\sqrt{\pi}}{\sqrt{2}}\left(\Psi(y_b)y_b\frac{\partial}{\partial y} + 2\Psi(y_b)y_b^2\right)F_0(y_b)$$

and shows excellent agreement.

4. Experimental comparison to flat-top scenario

A flattop scenario refers to the plasma current being in a steady state. This stable operation technique allows access to a robust RE population, which can be investigated in a more controlled and predictive manner than in cases of RE-generation during disruptions. Considering the relative importance of collisions and radiative effects on runaway dynamics, current flat-top plasmas are a close match to ITER post-disruption regimes.

4.1. Specific Frascati Tokamak Upgrade case

The Frascati Tokamak Upgrade (FTU) is a compact ($R = 0.935$ m, $a = 0.3$ m) device with high field configuration ($B_{tor} \leq 8$ T) [60] reaching plasma currents of $I_p < 1.6$ MA. In the pursuit to enhance mitigation schemes and control systems for tokamaks, a new measurement system, the Runaway Electron Imaging and Spectrometry (REIS), has been implemented [61]. REIS provides a measured synchrotron spectrum containing information about the runaway distribution. It is proposed, that an algorithm would then iteratively search for the best plasma parameters to fit the provided spectrum with spectra obtained by the SYRUP code [62]. The synchrotron emission is calculated by SYRUP using a distribution function, e.g. from CODE. The whole process is a non-trivial method, because it is an inverse problem: one searches in a 1D spectrum for a possible origin of a 2D distribution given. Several distributions can lead to similar synchrotron spectra. For the expensive iterative scheme to work, a good initial guess is required. The goal of the following work was to see, if the fast running linearized CODE is able to provide this initial guess, and if later it can be used for the iterative process. Otherwise, more expensive tools, such as LUKE [18] or NORSE [30], might be necessary. After receiving experimental data from the specific flattop-shot #39464 of FTU, CODE is applied on this data and investigated throughout. In parallel, it also served as a starting point for me to better learn the handling of CODE, before the more complex disruption cases treated in chapter 5.

4.2. Data Analysis

The experimental Data (figure 11) shows 8 graphs, 5 of which, namely toroidal magnetic field strength, line-integrated electron density, temperature, effective charge and parallel electric field strength, will be used as an input for CODE. Details about the diagnostics can be found in the paper by Esposito et al. [63] as well as in the references mentioned therein. One can compare the CODE-calculated value to the measured plasma current (figure 11a) and hereby verify the applicability of the simulation. Since the only RE measurement (figure 11e, see below) is qualitative rather than quantitative we do not compare direct runaway specific measurements. CODE evaluates the total current using the first Legendre-mode and integrating over the whole grid. To obtain the current carried by runaways, a mask is implemented, restricting the integration to the part of the grid, which meets the definition condition for REs. A current profile for the FTU measurement is given, obtained through equilibrium reconstructions. At the core, it

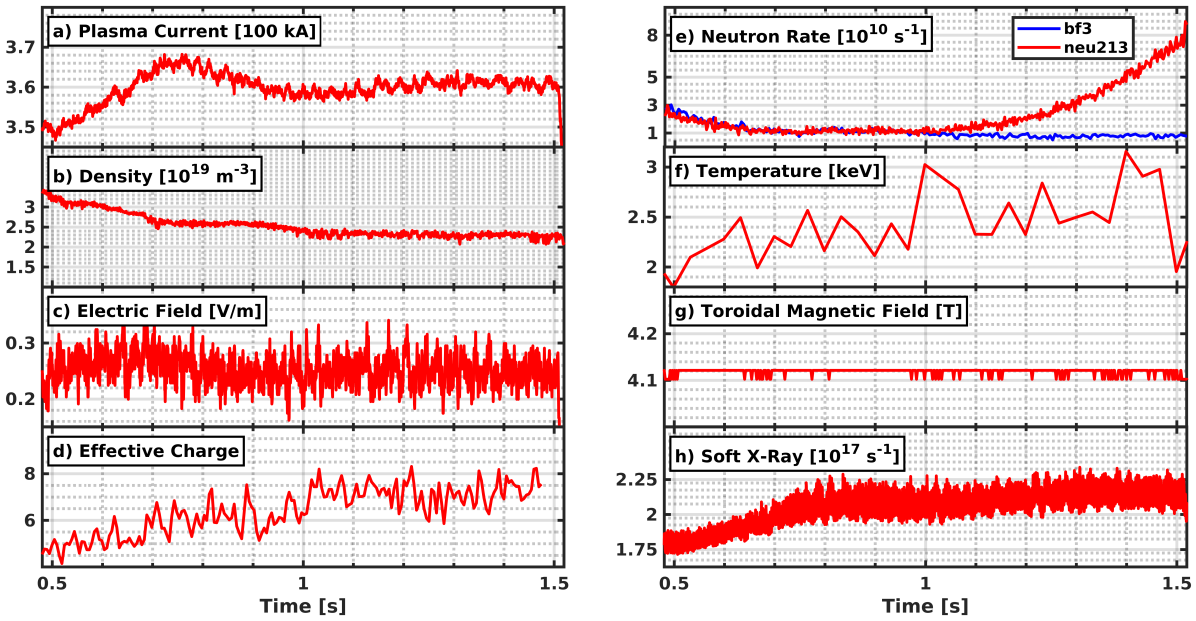

Figure 11: Experimental data from FTU shot number #39464. The x-axis corresponds to the time of the event in units of seconds.

varies from 3.4 to 6 [MA]. As reference value, the current $I_{\mathrm{FTU}} = 5$ [MA] will be set. The electron density (figure 11b) is given as core line averaged. The graph on the top right (figure 11e) shows measurement of a neu213-scintillator and a BF3 detector (boron trifluoride). The scintillator registers X-ray radiation as well as neutrons, while bf3 detects neutrons only. Since REs emit X-rays, the deviation of the neu213 measurement from the bf3-line increasingly shows the existence of runaways. The X-rays originate from bremsstrahlung, but it is not distinguishable whether from REs hitting the wall or colliding in the plasma. The temperature data (figure 11f) is obtained by Thomson scattering. I was told that the diagnostic has a tendency to produce oscillatory signals. Rounding errors in the analog-digital converter cause the recorded toroidal field signal (figure 11g) to slightly oscillate.

In order to use the data for my initial CODE calculations using time-independent input parameters, the arithmetic mean for line averaged density, electric field, effective charge and temperature in $t \in [0.5,\ 1.5]$ s is calculated. The mean values are

$$Z = 6.446, \quad n\ [10^{19}\ \mathrm{m}^{-3}] = 2.517, \quad T\ [\mathrm{keV}] = 2.444, \quad E\ [\mathrm{V/m}] = 0.253.$$

Also, a polynomial fit (figure 12) is done to obtain a basis for time-dependent plasma parameter runs. The magnetic field strength will hereby be considered constant at $B = 4.12$ T. For time-dependent calculations, 50 input data points are generated using the polynomial fit. The choice for the number of points is set in a way, that the resulting graph is smooth.

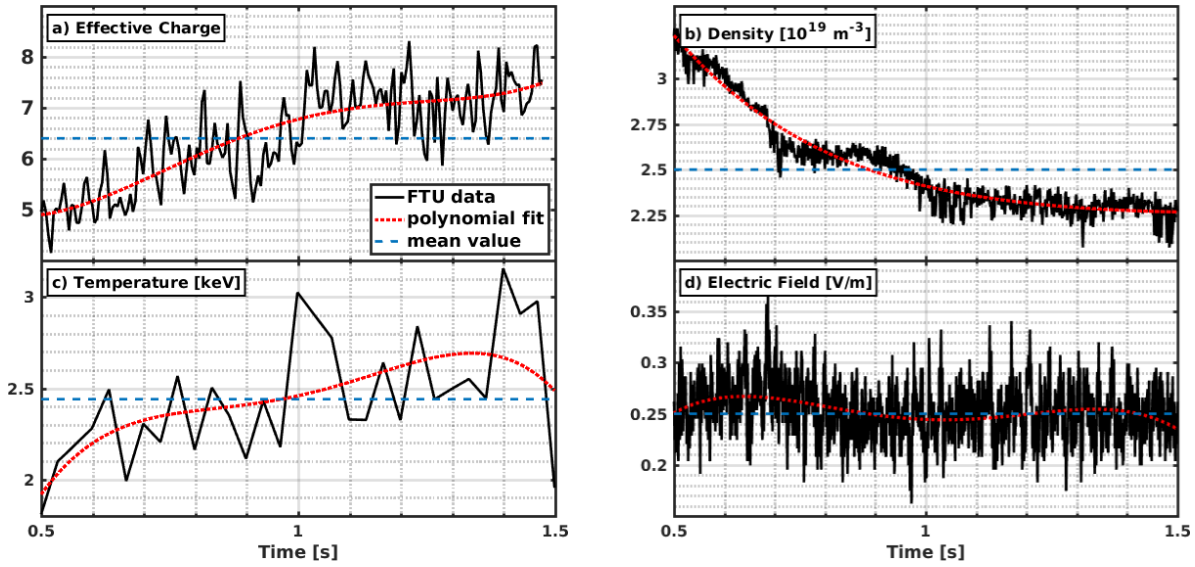

Fit properties $y = \sum_{i=0}^{4} p_i x^i$						Calculated data	
	p_0	p_1	p_2	p_3	p_4	mean values	
a)	12.62	-43.11	80.7	-58.06	14.61	Z	6.446
b)	6.38	-9-90	9.61	-4.35	0.77	n [m^{-3}]	2.517e19
c)	-6.22	35.86	-55.97	38.46	-9.67	T [keV]	2.444
d)	-0.57	3.85	-6.31	4.37	-1.09	E [V/m]	0.253

Figure 12: Physical input parameters for CODE as given by the experimental data of FTU shot #39464, plotted over time together with a polynomial fit (details in table) and the arithmetic mean. The arithmetic mean is used for both steady state and a time-evolving runs with constant parameters, while the polynomial fit deducts input data to run with time-dependent plasma parameters.

The plasma current, an integral quantity, is of special interest to the analysis. Therefore, if not otherwise stated, the energy-dependent Chiu source operator (see section 3.1.3) will be used as well as the relativistic test particle collision operator (see section 3.1.1). Latter is adequate for the purpose present, because we focus on runaways and do not estimate bulk quantities.

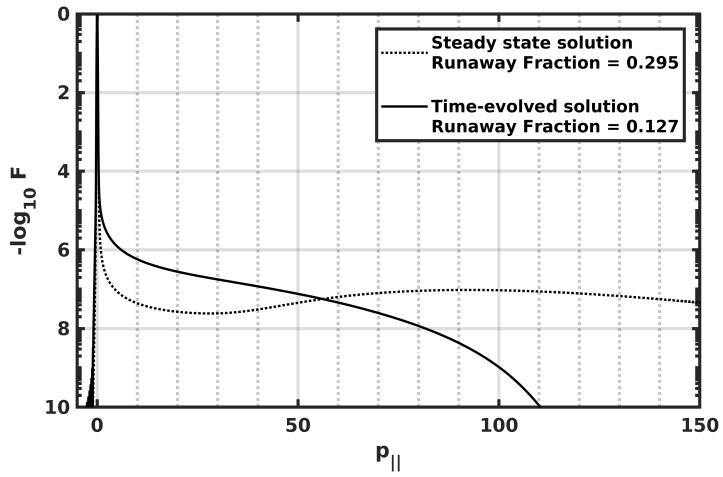

Figure 13: Arithmetic mean values as calculated in figure 12, processed by CODE in steady-state and time-dependent calculation with a duration of $t = 1$ s and $dt = t/100$. The runaway fraction is high, because the critical momentum $p_c \approx 0.3$ defining the runaway region is low for this case. For illustration reasons, the critical momentum is not displayed in this figure, but can be found as a pitch-dependent trajectory in the 2D-distribution in figure 15. Numerical input parameters are: $N_\xi = 125$, $N_y = 1950$ and $y_{max} = 1680$, and the Chiu avalanche operator S_{Ch} without pitch-dependence was used.

4.3. Steady-state calculations

Before time-evolution is considered, it is useful to calculate the steady state solution first and take a first glance at whether reasonable values for growth rate, runaway fraction and current are archived. It can be assumed, that the steady state results will overestimate the real event due to the timescale of the flattop-scenario (~ 1 s), up to which the equilibrium condition may not necessarily be reached.

Indeed, this I show in figure 13. Mean values from figure 12 for all parameters have been used, showing that after 1 second, which is the duration of the flattop scenario, the electron distribution has not reached steady state. The steady state solution has a non-monotonic feature, a *synchrotron bump* [47], which can be defined as particles piling up in momentum-space due to synchrotron losses increasing with electron energy (see F_{rad}, figure 3).

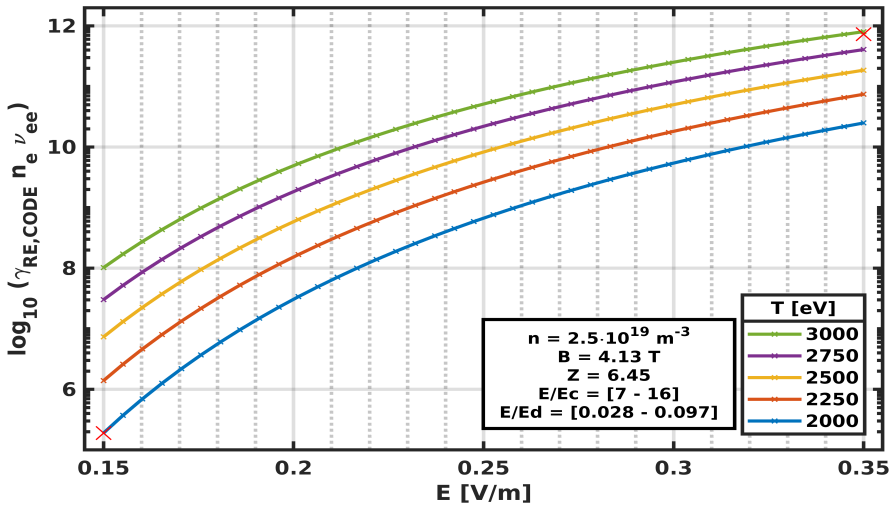

Figure 14: The growth rate for five different temperatures is plotted against a growing electric field strength to cover the whole range of parameters as given by the experimental data (figure 12). The y-axis is chosen such, because growth rate given by CODE is normalized to n_e and ν_{ee}. For the linearization of CODE to be valid, E/E_D must not overcome a few percent. Red crosses ((x)) indicate the value range obtained by eq. (21), verifying the CODE growth rate.

I carried out a wide parameter scan for all the important parameters to assess the sensitivity of runaway evolution and to study the effects of the measurement uncertainties. To take a first glance at possible results, a simple case is run, using the arithmetic means of the density, electric charge and magnetic field strength as calculated above. Electric field strength and temperature are used as variables covering the whole range of the experimental data, since the outcome is expected to be most sensitive to these two parameters. Without avalanche (which cannot be evaluated in a "steady state" calculation) and bremsstrahlung mechanism, the growth rate produces reasonable values and an asymptotic behavior (figure 14). It grows significantly with electric field and temperature, which affects in this case primary generation solely. For the purpose of validation, the runaway growth rate as calculated by CODE from the first Legendre-mode (see section 3.2.4) is compared to the relativistic Dreicer generation growth rate, as calculated by the commonly used Connor & Hastie formula [27]. Here the approximation uses the non-relativistic limit

$$\frac{dn_{\mathrm{NR}}}{dt} \equiv \gamma_{\mathrm{NR}} = C n_e \nu_{th} \epsilon^{-\frac{3}{16}(1+Z_{\mathrm{eff}})} \exp\left[-\frac{1}{4\epsilon} - \sqrt{\frac{1+Z_{\mathrm{eff}}}{\epsilon}}\right] \tag{19}$$

to obtain the relativistic case

$$\gamma_{\mathrm{R}} \propto \gamma_{\mathrm{NR}} \exp\left(-\frac{T}{m_e c^2}\left[\frac{1}{8}\epsilon^{-2} + \frac{2}{3}\epsilon^{-3/2}\left(1+Z_{\mathrm{eff}}\right)^{1/2}\right]\right), \tag{20}$$

$\epsilon \propto T$	$\gamma_R\left(Z_{\text{eff}}=6.45\right)/\gamma_R\left(Z_{\text{eff}}=1\right)$
0.010	0.000215
0.025	0.0106
0.050	0.0596
0.075	0.116
0.100	0.164

Table 1: Growth rate in the approximation of Connor & Hastie [27] for various temperatures. It shows how impurities in the plasma composition (Z_{eff}) change the primary growth rates of runaway population. At roughly $\epsilon = 0.1$ the linearization of CODE is expected to be broken.

where C is an constant of order unity, undetermined by the analytical model,

$$\nu_{th} = \frac{n_e e^4 \ln\Lambda}{4\pi\epsilon_0^2 m_e^2 v_{th}^3}$$

the thermal collision frequency of electrons with their own species, and $\epsilon = E/E_D \propto ET$. The range of temperature and electric field strength provides $\epsilon = [0.028 - 0.097]$ (figure 14). Calculating γ_R for this very range using eq. (20), yields

$$\frac{\gamma_R\left(\epsilon = 0.097\right)}{\gamma_R\left(\epsilon = 0.028\right)} \approx 3.1 \times 10^6, \tag{21}$$

and is drawn into the figure as red crosses, backing the numerical results. Runaway generation is nonlinearly sensitive to these crucial plasma parameters (E and T). The formula for Dreicer growth rate does not take losses into account, therefore the bremsstrahlung operator was disabled for this plot. Synchrotron losses are not taken into consideration either, but as was mentioned in section 3.2.1, its direct influence on the runaway growth rate is mostly insignificant. The saturation in this primary generation only plot is mathematically speaking due to the fact, that the growth rate in eq. (20) is exponentially suppressed with $\epsilon \propto ET$, which is seen in the converging curves for both electric field strength and temperature.

Due to the unusually high effective charge in this FTU-scenario ($Z_{\text{eff}} = 6.446$), it is of special interest to consider the effect of impurities on the plasma. Evident from eq. (20), the plasma composition does not only affect bremsstrahlung losses [64] (see eq.(15)), but also directly reduces the primary growth rate of runaway electrons. Table 1 demonstrates how the production of runaways is influenced by this degree of impurity for various temperatures. The effect originates from electron-ion collisions. Even assuming fully elastic interactions with the ions, the pitch-angle deflection effectively hinders the electric field acceleration, since latter has a preferred direction.
The accumulative change in momentum due to electron-ion collisions can be described as [5]

$$\left\langle \frac{\delta p}{\delta t} \right\rangle_{coll}^{ei} = -\frac{p}{\tau_{ei}} \propto Z_i^2 T^{-3/2} \tag{22}$$

using the electron-ion momentum relaxation time

$$\tau_{ei} = \left(\frac{4\pi\epsilon_0}{e^2}\right)^2 \frac{3\sqrt{3m_e}T^{3/2}}{4\pi Z_i^2 n_i \ln\Lambda}$$

for an ion number density n_i. It has to be noted that the latter expression of proportion $\propto T^{-3/2}$ in eq. (22) is not strictly true, since $\Lambda \propto T^{3/2}$ holds, but this can be neglected reasonably in the logarithm.

So given the assumptions above, the negative effect that impurities have on the growth rate of runaway electrons fade significantly with electron temperature.

4.4. Time-evolved calculations

Since it has been shown that the steady state calculations overestimate the evolution of the distribution, the next logical step is to consider a time-evolving system with constant plasma parameters. The question of efficiently choosing numerical parameters has been eased with the knowledge from my previous study. Limiting the run to the duration of the flattop scenario of 1 s and taking the mean plasma parameters as calculated in figure 12, the runaway fraction, total and runaway current evolve as shown in figure 15a. Nearly all the current is driven by runaways by the end of the calculation. Below, the final distribution after 1 s in 2D momentum-space is shown. The Chiu source operator and mean stopping force bremsstrahlung operator have been used. Neither account for pitch dependency, but since the quantity of interest is an integral one, calculation time can be saved using these simpler operators.
The total current density $j_{\mathrm{tot}} \approx 1.48{\cdot}10^8$ [A/m^2] output by CODE, vastly exceeds the measured value of $j_{\mathrm{FTU}} = I_{\mathrm{FTU}}/\pi a^2 \approx 5{\cdot}10^6$ [A]$/\pi a^2 \approx 1.77{\cdot}10^7$ [A/m^2] by one order of magnitude. To see if this discrepancy can be sorted out, the plasma parameters themselves will be considered time-dependent in the next step. Since runaway dynamics are of interest to this thesis and $j_{\mathrm{RE}} \approx j_{\mathrm{tot}}$ in the calculations, focus will be laid on the runaway current from now on.

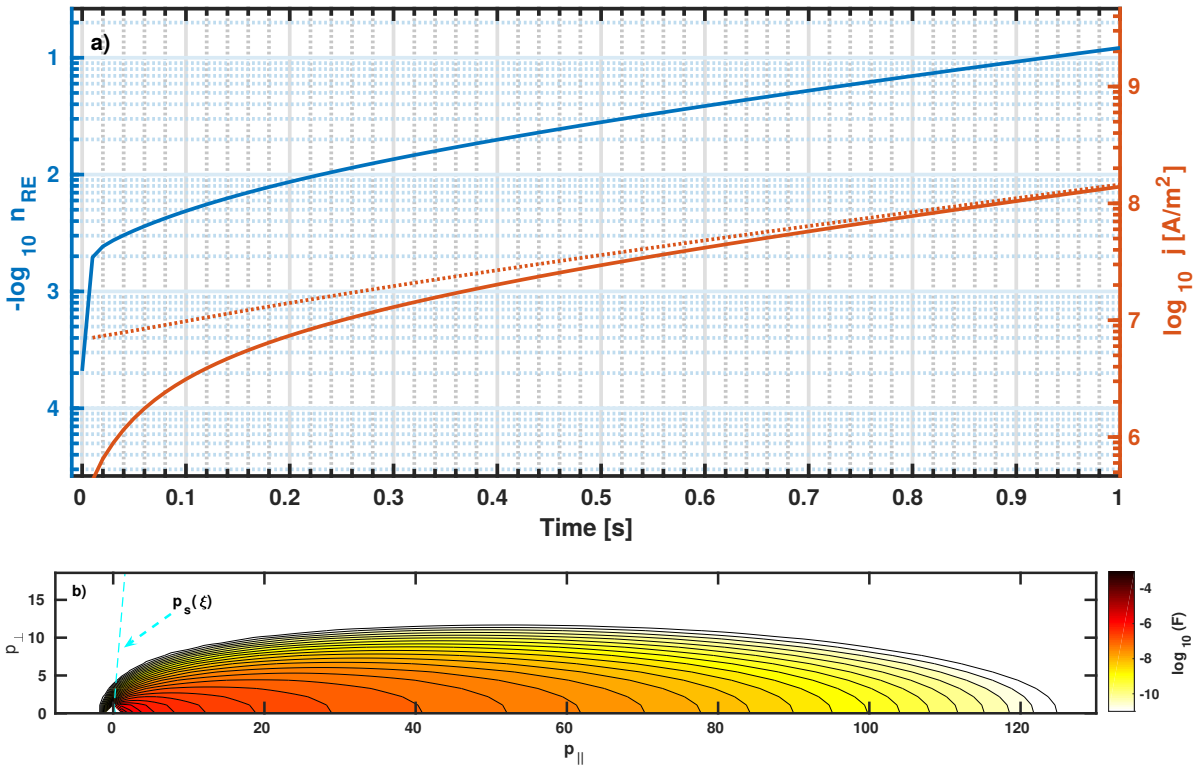

Figure 15: Final distribution function (b), runaway fraction, total (dashed) and runaway (solid) current density (a) of shot #39464 in time advance. After 1 s practically all of the current is driven by runaways. $p_s(\xi)$ resembles the pitch-dependent trajectory defining the runaway region. The energy-dependent Chiu source operator has been used and a mean stopping force bremsstrahlung operator. The numerical parameters and operators are chosen as in figure 13.

4.5. Time-dependent plasma parameters

Time-dependent plasma parameters significantly increase the computational time of the simulation. Every time a parameter changes, the differential operator matrix representing the system needs to be rebuilt and refactorized. Whether the additional computational cost is justified, will be seen by the impact of the time evolution of the plasma parameters T, Z, E and n. One by one, the influence of their time-dependency on runaway fraction and runaway current is investigated (figure 17(a-d)). Figure 12 containing the time-dependent parameters is replicated in figure 16 to ease the read.

The polynomial fit for the electric field oscillation measured (figure 16a) does not deviate much from the arithmetic mean and nor does the runaway fraction for the time-dependent E-input (figure 17a). The similarity has the benefit, that the definition of "runaways" is consistent throughout the calculation, and the introduction of "fast particles" is not necessary. The comparatively high density at the beginning of the flattop-scenario (figure 16b) effectively suppresses runaway growth rate ($E/E_C \propto n_e^{-1}$, $F_B \propto n_e$), leading to the runaways only carrying a calculated current of $2.5{\cdot}10^8$ [A/m] after one second (figure 17b). Similar behavior is shown by the temperature scan (figure 17c). Here, the below average T (figure 16c) negatively influences the Dreicer growth rate ($E/E_D \propto T$). Quite the opposite trend is observed with the time-dependent effective charge Z_{eff} (figure 17d). Turning the bremsstrahlung operator off does not significantly effect the outcome, so the influence is mostly due to electron-ion collisions.
From the figures it seems, that the runaway growth rate is most sensitive in the initial phase and requires time-dependent treatment especially when the deviation from its mean is in the beginning of the calculation. Looking further into it, I repeated the density and temperature scan (figure 17(f-g)), but the time-axis reversed (backwards in time). This way, the overall deviations from the average remain the same, but the initial phase of the runaway generation is subject to respectively below average density/temperature. The influence on the simulation results are significant. The question, whether there is demand of time-dependent treatment of the plasma parameters, is answered most easily during the early behavior of the parameter in question.

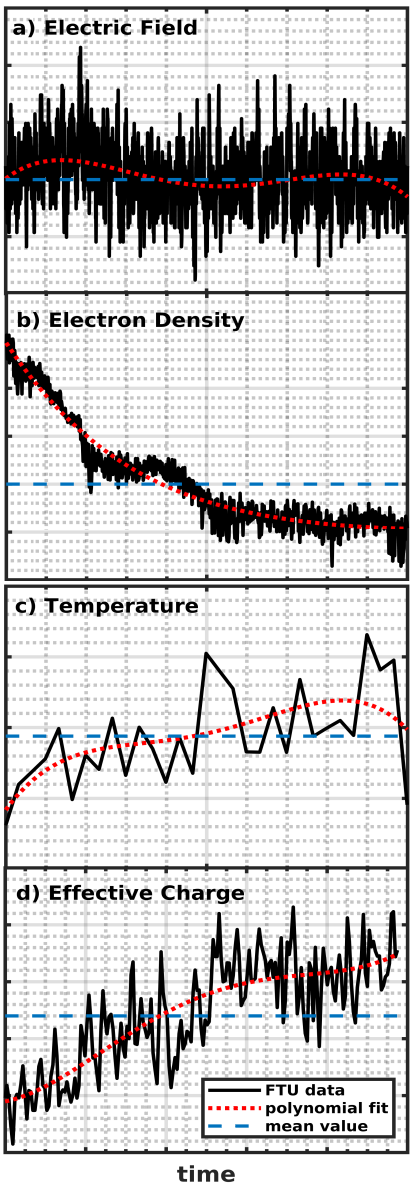

Figure 16: Blank repetition of figure 12.

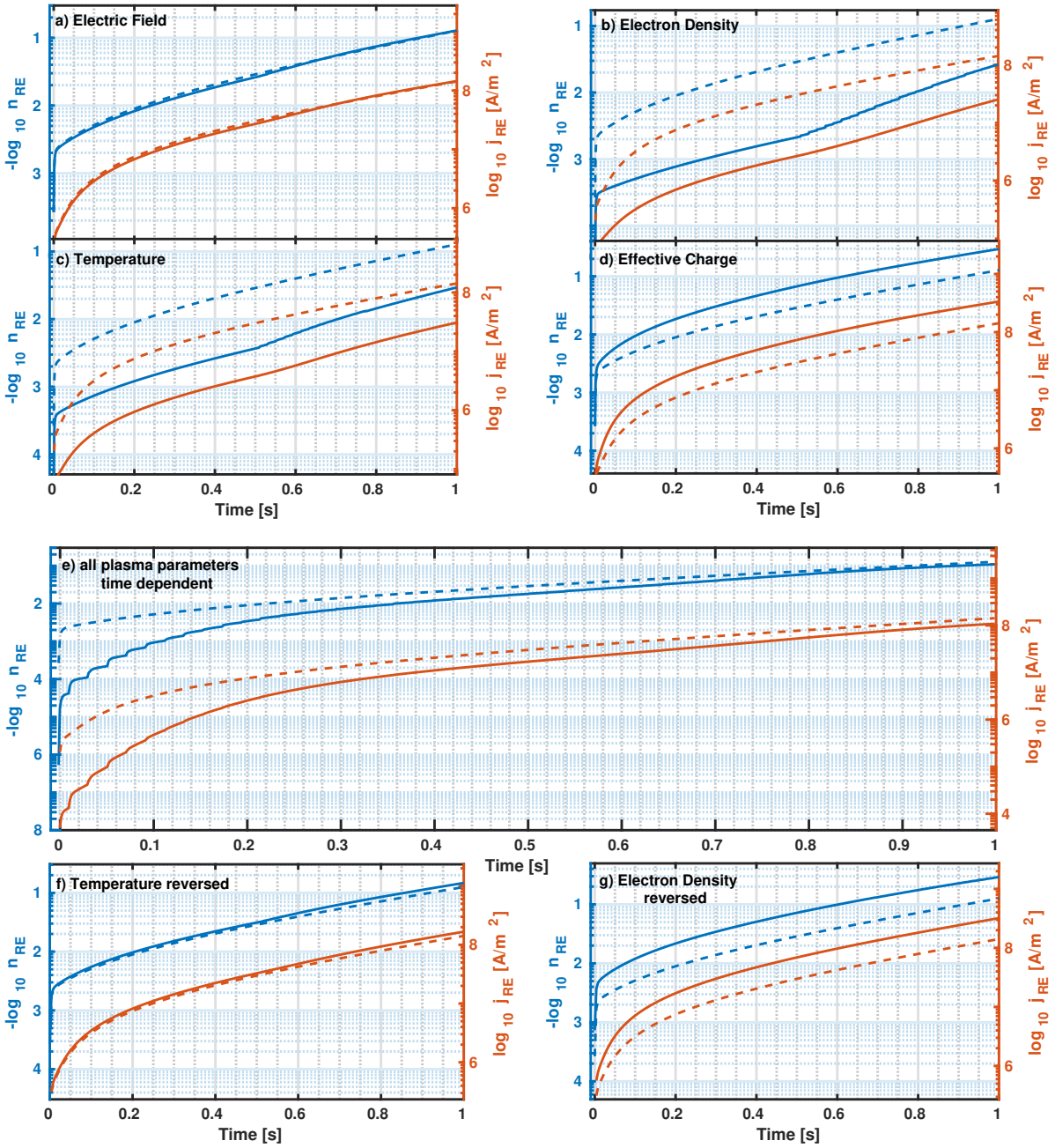

Figure 17: (a-d): Biaxial plots of runaway fraction and runaway current density for the particular plasma parameter input time-dependently as given by the polynomial fit (continuous line). A simulation for all plasma parameters simultaneously being time-dependent is shown in (e). For reference, the time-evolved solution with mean values is always depicted (dashed). The input parameter that is being referred to can be found in figure 12. (f-g) shows the same procedure for density and temperature, but with the time-direction reversed.

Even though the time-dependency of electron density, temperature and effective charges is found to be influential, the combination of all seem to cancel out in the case of FTU shot #39464 (figure 17e). The desired value in runaway current density is still overstated by roughly one order of magnitude.

The runaway generation in the regime investigated is highly sensitive to the electric field at this point. A reduction of the electric field by 15% to $E = 0.22$ V/m reproduces the desired current (see figure 18, black dashed line) and leads to a more reasonable $E/E_D = 0.0487$ for small tokamak devices. Further focus to explain the discrepancy has been laid onto the high effective charge.

First, a scan for various Z_{eff} has been produced to quantify the influence of the charge and is depicted in figure 18. Remaining plasma parameters are set to their mean ones, independently in time, as it has been shown that the effect of their combined time-dependency is minor (figure 17e). The results strain across many orders of magnitude and a converging behavior for growing Z_{eff} is observed. An effective charge of $Z_{\text{eff}} \simeq 10$ would be required to reproduce the current of FTU, roughly twice the value measured. In the pursuit of finding the origin of the overestimation of the current, various combination of settings had been tried out. The Chiu and Rosenbluth-Putvinski source operator are compared in figure 18. The statement, that the Rosenbluth-Putvisnski operator can collide electrons to an energy higher than that of any of the electrons available (section 3.1.3), has to be kept in mind looking at figure 18b. Contrary to that, the Chiu operator (figure 18a), which is assumed to be generally more valid, takes the energy distribution into account. Not creating the aforementioned (unphysical) high energy particles does seem to allow the electron distribution to reach an equilibrium for high effective charges. In the regime of $1 \leq Z_{\text{eff}} \leq 10$ the variation due to the source operator is however barely noticeable (figure 18c). The difference in the Z regime above that is larger, up to a factor of ~ 30 for $Z_{\text{eff}} = 40$, but declines again for charges higher than that. The same trend is reproduced when turning the bremsstrahlung operator off.

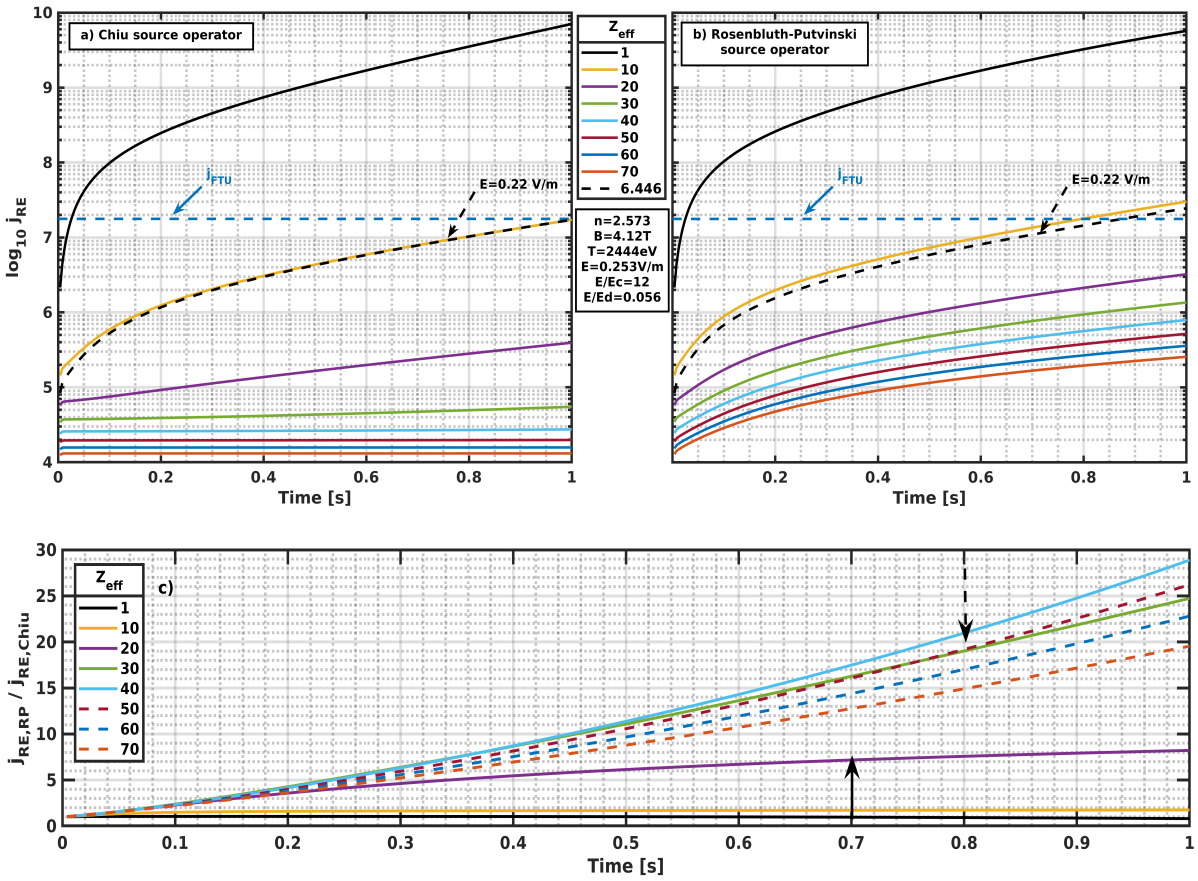

Figure 18: Scans for high effective charges with the Chiu (a) and Rosenbluth-Putvinski (b) avalanche operators (see section 3.1.3). Density n is given in 10^{19} m^{-3} and the y-axis shows the logarithmic values of the runaway current density in [A/m]. Also included is the reference FTU-current density $j_{\mathrm{FTU}} = 1.77{\cdot}10^7$ [A/m^2] and an attempt to reach it by reducing the electric field strength (black, dashed line for $Z_{\mathrm{eff}} = 6.446$). Graph (c) shows a comparison of both operators by dividing the current densities from above through each other. The continuous arrow indicates the difference growing with Z, the dashed arrow illustrates the trend decreasing again for $50 \leq Z_{\mathrm{eff}} \leq 70$.

It came to suspicion that a high tungsten ($_{74}$W) concentration, scraped off from the plasma-facing components, might be present in the fusion plasma. In the temperatures available, tungsten is not fully ionized [65]. This could significantly change the electron dynamics: Heavy ions, not fully ionized, have to be accounted for as partially-screening [66]. High-energy runaways are hereby subject to the internal electron structure of those still bound, experiencing an increased damping strength. This was thought to be the mechanism able to explain the overestimated runaway current density. Calculations to determine the number density of tungsten particles and their ionization state had been started to simulate the FTU case with partial-screening. However, before these could be finished, it was confirmed, that actually the source of high-Z in this discharge was $_{42}$Mo-impurity, and not W. Taken from figure 1b in [67], the ion charge of molybdenum at a temperature of roughly 2500 eV estimates at about 32. With only 10 bound electrons, Mo^{32+} is better represented by the Z_{eff} than W would be. At this point, the effect of screening would put the effect between using $Z_{\text{eff}} = 32$ and $Z_{\text{eff}} = 42$ and as shown in figure 18 the difference is only a factor of $\sim 2\times$. Also, accurately calculating the effect is not possible, since the atomic data (obtained by density functional theory calculations) necessary to account for the screening effect, is not yet available [68].

At this point, no further reasons were found to explain the overstatement of the runaway current-density by CODE, except that the 0D approach might not be applicable to this flattop case. Due to the comparably low generation of REs in flat-top of small tokamak machines like FTU, even relatively small loss rates, which would be negligible in disruption scenarios, might become comparable to the generation rate. The importance of transport of runaways, not covered by CODE, has to be discussed.
Weak loss of particles due to magnetic perturbations have been reported for post-disruption cases in JET [69], as well as threshold effects for particle transport losses in ITER-like plasmas (see Papp et al. [70] and Féhér et al. [71] and the references therein). For flap-top operations specifically, the research topic is still under current investigation. A team working with the 1D Fokker-Planck-solver LUKE on flat top runaways, has – in parallel to our work – quantified the importance of diffusion of particles on the runaway current for the TCV tokamak [72] (which is similar in size to FTU). During a 1 s simulation, the runaway current j_{RE} seemed to roughly scale with the radial diffusion coefficient D_r as

$$j_{RE} \propto D_r^{-3/2}. \tag{23}$$

The diffusion coefficient $D_{r,m}$ due to magnetic perturbations can be estimated e.g. by using the work of Hauff and Jenko [73], where the coefficient is evaluated for TEXTOR parameters (best comparable to FTU from the cases presented in the paper) as a function of kinetic energy. For the time-evolution simulation using mean values (see figure 13), the average runaway energy as given by CODE, reaches ≈ 13 MeV. Assuming turbulence similar to the one in the aforementioned study [73] I can estimate the diffusion coefficient to reach values as high as ≈ 20 m^2/s (peaking at roughly 0.3 MeV). Runaway electrons are very sensitive to transport processes due to their velocity. With eq.(23), this would mean a decrease in runaway current because of transport down to 1%, in comparison

to a case with no transport at all. The effect of transport on RE seed generation is an open question and currently under research (see e.g. papers by Sarkimaki [74] and Sommariva [75]).

4.6. Conclusion

CODE has in its history been successfully applied to many scenarios. There are cases where a linearized Fokker-Planck solver can be applied, and for these cases the comparatively fast run-times of CODE is an advantage over more complex tools. Particle and energy loss due to transport processes, which are not captured by CODE, did not seem to limit its applicability on big tokamak disruptions[66], as the high runaway generation rate outweighs particle diffusion for most of the duration of the disruption[75]. The idea of simulating electron distributions on the compact tokamak FTU required an efficient solver, since a fast computation was desired when iteratilvey fitting measured synchrotron spectra with forward calculated ones. For the data given, CODE however could not reproduce the plasma current and overstated it by one order of magnitude. On the other hand, due to the high sensitivity of the runaway growth rate in this parameter regime, just a slight change of the electric field by 15% is capable of matching the measurement. The possibility of measurement errors should therefore be investigated. Otherwise it turns out, that the 0D limitation was less justified on FTU due to the runaway generation being comparable in its magnitude with the radial transport of particles [72].
Based on this work and as long as no measurement errors can be confirmed, we would recommend to employ CODE for the suggested synchrotron measurement fit with caution. It could become a better possibility, once e.g. a "local transport" model is implemented, or if the iteration is started with altered plasma parameters. As I showed, a slight reduction of the electric field, or an increase in Z_{eff} can be enough. A more complete model using a 1D Fokker-Planck solver can be obtained, if reasonable estimates about the transport can be given.

5. Disruption cases

The FTU-scenario as given in chapter 4 is considered to be a flattop-case. This section, however, is dealing with a disruption scenario, and its purpose is to show up to which extent CODE, with its linearization, is applicable to disruptive scenarios.

For tokamaks of size comparable to AUG or larger, a full current quench with full-f kinetic tools using self-consistent electric field has not been simulated yet. Research has been done either on smaller sized tokamaks (e.g. TEXTOR [49]) or with delta-f methods [40], where the distribution is not resolved as a whole, but split into thermal and superthermal (RE) parts. The plasma parameters in the simulations to come are therefore set to be typical to AUG disruptions, especially taking the specific cases of shot #33939 and #34075 into reference.

Simulations for big tokamaks have been attempted using nonlinear tools (NORSE [30, 31]), but it was found, that the feedback mechanism provided by the self-consistent treatment is highly dependent on the exact details of the heat sink mechanism. A disadvantage of nonlinear kinetic solvers is that the kinetic equation matrix has to be rebuilt in every iteration step (i.e. at every thermal collision time) which makes these simulations significantly more expensive than linearized solvers. It is therefore of interest, to investigate at which point a nonlinear treatment becomes an unavoidable necessity. The goal of this section is to investigate, up to what degree can we model a quench scenario in an AUG sized machine using linearized tools, and at which point simulations break down. We can envisage a hybrid approach for the future, where the initial stages of the evolution are followed by a linearized Fokker-Planck solver, and the more expensive nonlinear solvers take over the calculations just when it is necessary.

In this section I will present simulations of thermal and current quenches for a tokamak (see section 2.3). For this purpose, (a) initial distributions have to be created, (b) an attempt to model a disruption using externally supplied electric field evolution is being made, followed by (c) the introduction of self-consistent treatment of the electric field. A fully inclusive evolution of the disruption would require a self-consistent treatment of the background plasma as well [76, 69], but is out of the scope of this thesis.

5.1. Creating an initial distribution to disrupt

For the purpose of being more controlled and easier to reproduce, a distribution is initialized separately, which, for the disruptions to follow, will be used as a starting point. This corresponds to a "flat-top" current carrying distribution, which is then forced to undergo a thermal quench. In order to do so, a Maxwellian with $j = 0$ shall be exposed to an electric field, to drive a $j \neq 0$ Ohmic current. To keep calculation times tractable also in later stages, the grid should be kept as small as possible, while still providing the necessary resolution. Since we consider a regular flat-top initial distribution, the pres-

ence of a high energy tail is not necessary. As the possibility of steady-state solution is not implemented in CODE for the fully conservative collision operator, a time-dependent calculation is necessary, using a low electric field, slowly evolving to the desired current density. The collision operator of choice in this chapter is the momentum-conserving, non-relativistic field-particle term (see section 3.1.1), as we are interested in the distribution bulk response (see section 5.4).

MGI-induced post-disruption runaway electron generation has been sporadically observed on AUG at a central electron temperature as low as ~ 1.3 keV (#34075). The typical runaway scenario on AUG however reaches ~ 10 keV core temperature, to aid RE generation (see the example presented in figure 4). I will present three different initial distributions with initial temperatures of $T_{e0} = [1, 2.5, 5]$ keV. A 10 keV initial distribution has also been created using CODE, but could not be fully processed (due to limits in available computational time) until the thesis deadline. The validity of using a non-relativistic field particle operator at a $T_e \sim 10$ keV high temperature distribution has not been evaluated. Creating it in the first place required addition of the relativistic test-particle operator, which also required a sizable grid and smaller time-stepping, as a significant amount of bulk-particles (test-particles) become relativistic.
Three distributions ($T_{e0} = 1$ keV) deformed by various electric fields are shown in figure 19. The discrepancy between the current (a) calculated though the Spitzer-conductivity (eq.(13)) and (b) obtained from CODE-output (first moment of the distribution function) grows, as the electron population bulk is distorted. Current, which is expressed as the first moment of the distribution, stems from asymmetry in the distribution.

A radial *average* current density typical for AUG is of order 10^6 [A/m^2]. With the current profile peaking at the axis, which is also where the runaway generation most dominantly takes place, I choose the current density of $5{\cdot}10^6$ [A/m^2] according to the $E/E_C = 5.25$ case in figure 19 for all three of my initial distributions. Although $E > E_C$ creates a number of runaway electrons ($\approx 10^{-13}$) for $T_e0 = 1$ keV, the grid can be kept small sized due to their number and current being negligible.

At first I validated that the distribution would rearrange to a $j = 0$ Maxwellian in the absence of an electric field. This also provides the reference to the current relaxation without an induced electric field (e.g. a uniform plasma). The current density evolves as shown in figure 20, when continuing the distribution without external and no self-induced electric fields. For the high-temperature distributions the current takes longer to settle. Current is being caused by an asymmetry in the distribution, and under equal circumstances the reshaping to the (symmetric) Maxwellian takes more time when the initial temperature was higher.

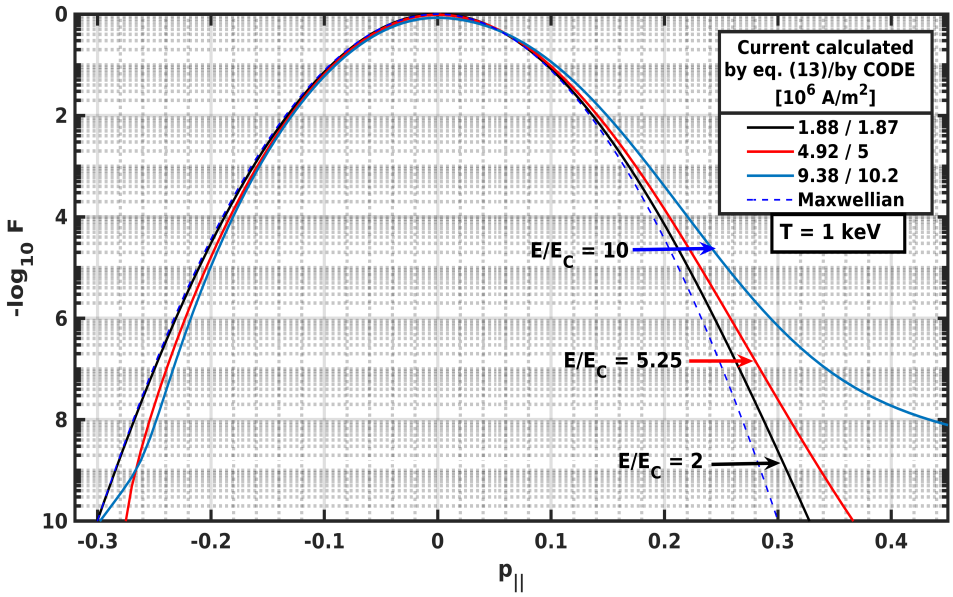

Figure 19: Distribution functions as distorted from their $j = 0$ symmetric Maxwellian forms by various electric field strengths. The legend contains the output total current density (as given by the first moment of the distribution) as well as the current density calculated by eq. (13). Input parameters are: $T = 1000$ eV, $B = 0$ T, $n_e = 3 \cdot 10^{19}$ m^{-3}, $Z = 1$, $N_\xi = 20$, $N_y = 90$, $y_{max} = 8$, $t_{max} = 5000$ $[1/\nu_{ee}]$ and $dt = t_{max}/350$. Back-tail scattering as already observed and explained in figure 9b is again observed on the negative momentum axis for the $E/E_C = 10$ case. The reference Maxwellian on the negative side of the momentum scale is overlapped by the $E/E_C = 2$ line.

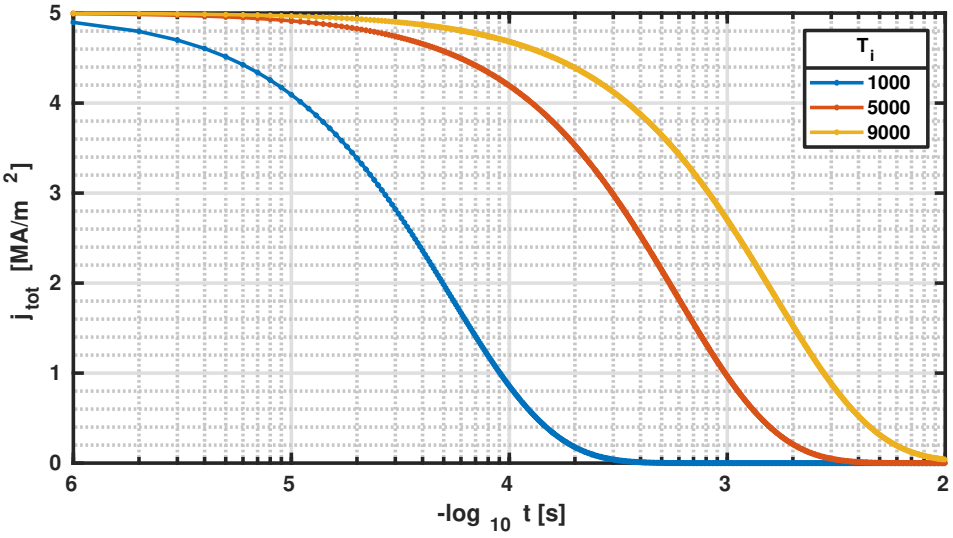

Figure 20: Drop in current density on a logarithmic timescale for the three initial distributions without self-induced electric field feedback, no external electric field, using the momentum-conserving collision operator.

5.2. Disruption events with measured electric field

As both temperature and electric field strength are usually observed during a disruption, one could try to model such a scenario with CODE, using the measured $E(t)$ as an external field input. Data for $T(t)$ and $E(t)$ from AUG shot #33108 (figure 4) will be used to demonstrate the issues arising with this approach. Thermal and current quench, as well as the fitted graphs are shown in figure 21a. Note that the initial temperature in the actual AUG discharge is higher, because I only show a clip of the whole scenario (and on a different time axis).

There are multiple issues with using experimental parameters. First is the spatial inconsistency. The temperature profile evolution can be measured with reasonable spatiotemporal resolution and accuracy, thus making the core $T_{e0}(t)$ evolution available. On the other hand, electric field is either calculated in a 0D fashion, or is measured via voltage loops at the plasma edge. The other issue is the temporal inconsistency. Since any electric field measurement or evaluation is global, this can cause a time delay between the measured temperature and the electric field evolutions. Furthermore, experimental jitter and time sampling issues can also be present. The fundamental issue is when the supplied electric field is too low compared to the temperature provided for the given time point, there will be no RE generation in the simulation. On the other hand, if the electric field is too high for the respective measured temperature, significant RE overproduction (and even immediate slide-away) can occur. The time delay between these two quantities can therefore set the RE conversion virtually anywhere between 0% and 100%.

To illustrate this effect, I represent the time lag between measured $T_{e0}(t)$ and $E(t)$ by an offset in the data points obtained for a fit onto both parameters. The offset of one data point equals roughly 0.09 ms. Dreicer runaway generation, being dependent on $E/E_D \propto ET$ can be influenced heavily when shifting e.g. the peak electric field closer to the initial temperature (figure 21b). The values obtained here ($E/E_D > 1$) would even create an immediate slide-away (see section 2.2). It is problematic to resolve this spatiotemporal inconsistency between the input parameters, which makes the use of direct experimental data complicated, and a self-consistent modeling of the electric field becomes necessary.

As a first step, a "quasilinear" treatment will be followed, for illustration purposes. Here we are going to use an electric field evolution calculated self-consistently for a given temperature drop using the 1D "fluid" disruption-runaway code GO [69], and feed it as input to CODE in time-dependent mode. Although self-consistent coupling of GO and CODE had been implemented earlier [76], using that model – which also requires significantly larger computational resources – is outside the scope of this thesis.

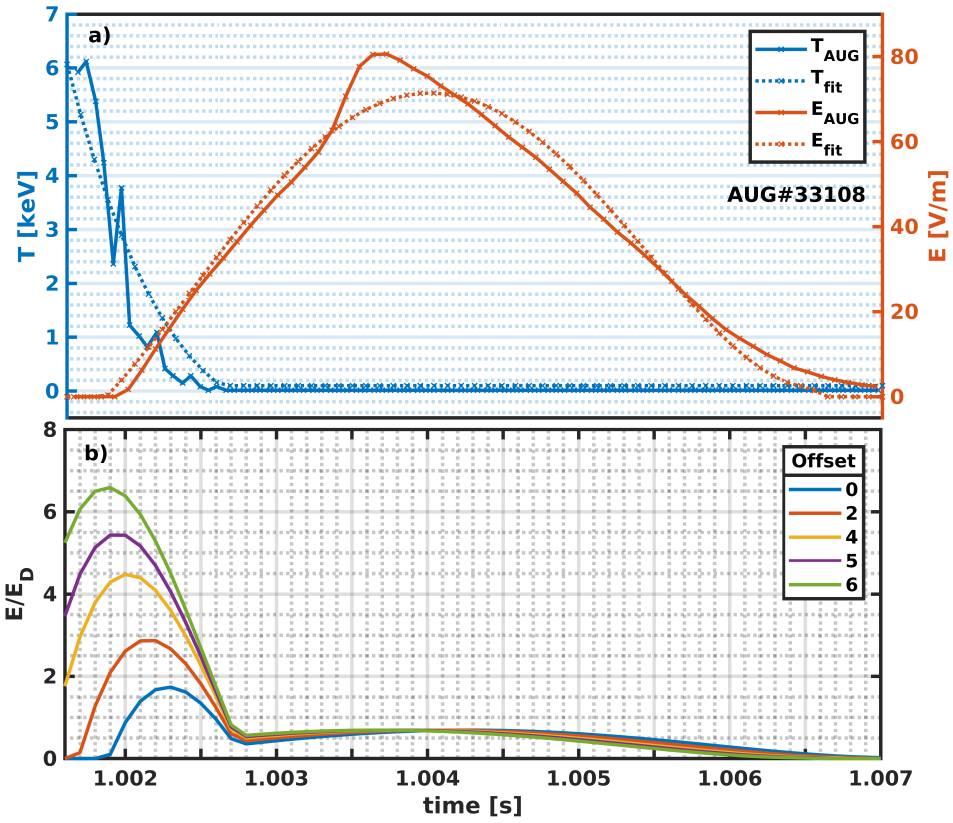

Figure 21: (a) Electric field and temperature evolution during thermal and current quench of AUG shot #33108 (figure 4). Dotted lines are the fitted graphs, represented by 60 data points. Figure (b) shows $E/E_D \propto ET$ with various offsets in the data. An offset is the amount of data points, by which the electric field is shifted left on the x-axis. As the 60 data points are equidistant and the total duration is 0.53 ms, an offset by 1 means an offset by roughly 0.09 ms.

5.3. GO code calculated self-consistent electric field input

GO is a 1D-tool, capable of computing the evolution of the radial electric field profile during runaway evolution (approximated by "fluid" generation rates) self-consistently [69]. For a distribution with an initial temperature of $T_{e0} = 1$ keV, an exponential temperature drop to $T_f = 1$ eV is prescribed in time t via

$$T(t) = T_f + (T_i - T_f)\exp\left(-\frac{t}{\tau_0}\right),$$

where τ_0 is the exponential decay time, chosen similar to the thermal quench timescale. As CODE assumes a uniform (0D) plasma, the obtained E-field evolution $E(t)$ is taken at a constant point in space (near axis). Choosing $\tau_0 = 0.25$ ms, the electric field response to the drop in current originating from the rising resistivity due to temperature decay, is shown in figure 22a.

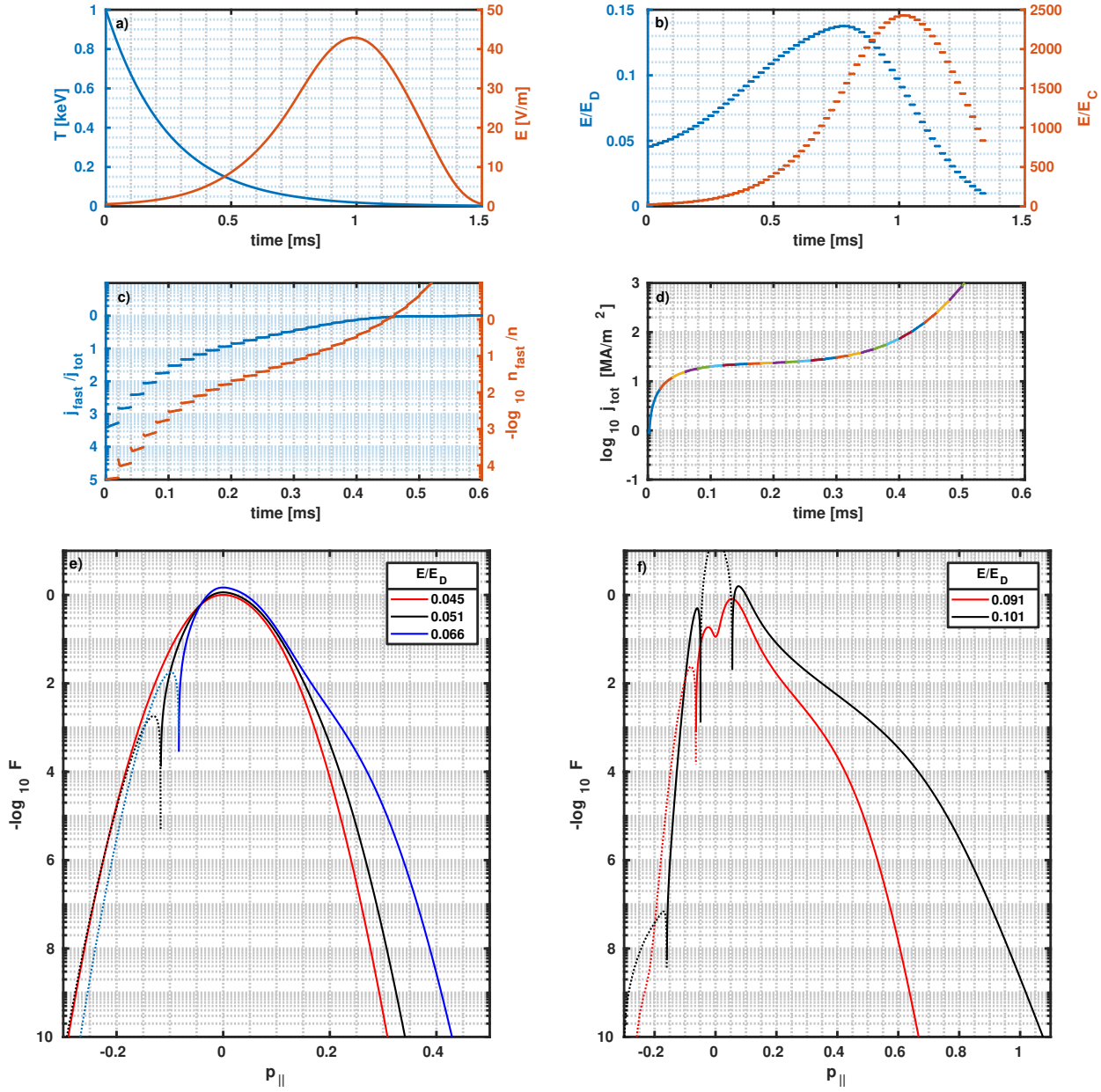

Figure 22: (a) Shows the input to CODE as obtained by the GO code, (b) the normalized electric field outputs by CODE, (c) the fraction of fast particles and the fraction of current carried by them, and (d) the total current density. Note that (c) and (d) are depicted on a shorter time scale. In (e) and (f) illustrated are the first few distribution functions on the parallel momentum axis. Negative values are generally depicted with dotted lines. Input parameters are: $n_e = 3{\cdot}10^{19}$ m^{-3}, $Z = 1$, $B = 3$ T, $N_y = 5000$, $N_\xi = 50$, $y_{\max} = 50$ and $dt = t_{\max}/200$. The combined non-relativistic field particle and relativistic test particle collision operator was used, as well as the Chiu source operator without pitch-dependency.

Modeling a disruption case with CODE has to be done with care due to the usage of reference temperature (see section 3.1). Physically, the reference temperature relates to the background plasma temperature. The grid normalization is defined by the reference temperature $\bar{T}$. However, the actual temperature which describes the Maxwellian bulk in the collision operator uses the instantaneous temperature. To sustain numerical accuracy, the reference temperature should not be far from the instantaneous one. Due to the implementation, the reference temperature cannot be changed during one instance of a CODE run. As a disruption involves a temperature drop of many orders of magnitude, the reference temperature would have to be adapted continuously. For this purpose, CODE has to be restarted multiple times during the temperature drop (thermal quench), each time choosing the reference to be close to the instantaneous temperature, and continue the evolution of the distribution obtained in the time interval before. In this case, CODE has been restarted at every timepoint of $E(t)$, taking the instantaneous temperature as reference temperature.

Also required for evaluating disruptions, is the usage of "fast particles" (see section 3.1.3, last paragraph). As electric field changes in time, so does the definition of the critical momentum $p_c = \gamma v_c/c$, which is commonly being used to identify the runaway region. In order to avoid inconsistency through time and numerical instabilities, particles in momentum space with either (a) $v > 0.25c$ or (b) $f(p)/f_M(p) > 1000$ will be counted as "fast particles" instead of the regular definition of REs. Definition (b) represents the "tail" of the distribution, which has to differ from the Maxwellian f_M by a factor of 1000 and (a) can be seen in the distribution plots at roughly $p_\parallel = \gamma v_\parallel/c \approx 0.25$, depending on relativistic mass factor γ and pitch. The avalanche source operators which are usually restricted to a high-energy region above p_c in momentum-space (see section 3.1.3) are also adjusted to this definition.

Figure 22b shows the normalized electric fields E/E_D and E/E_C and how the restarting procedure affects the calculation. As dictated by the high values of E/E_D a significant runaway tail forms, bringing the distribution far from a Maxwellian, where the linearization is no longer valid. This eventually leads to unphysically high fast particle fractions $n_{\text{fast}}/n(t > 0.5\text{ ms}) > 1$ (figure 22c). This misbehavior stems from the linearized collision operator, and cannot be prohibited by any increase of numerical parameters. The overall current density stemming from the growing asymmetry of the distribution is illustrated (on a shorter time basis) in figure 22d.

Distribution functions for $\xi = 1$ are shown in figure 22e. Dotted lines show the absolute of actually negative values in the distribution as seen in the back-tail. Generally, this has not to be considered an error, since the linearized collision operator simply does not conserve positivity (without losing mathematical validity). Yet problems might arise, when the negative values cover a significant fraction of the distribution. The density conservation, trying to maintain the normalization, over-corrects the positive part of the population, as seen by the distributions exceeding $F(p = 0) = 1$. As the electric current is heavily influenced by the asymmetry of the function, a slight change in the densely-

populated bulk has a significant impact on the current density (figure 22d). A current quench is not observed, instead the current rises by up to 3 orders of magnitude. Since a fast-particle fraction of below 1% is generally handled correctly by CODE, it is assumed that the negative back-tail and the subsequent rise of the distribution, troubles the result. Increasing time or space resolution does not get rid of them. Those appearances will have to be watched out for carefully.
As we see, it is necessary to calculate the electric field self-consistently with the evolution of the distribution within CODE itself. However, based on the above examples we can expect that for AUG-like disruption cases the linearization of CODE might break down.

5.4. Disruption events with self-consistent electric field treatment

In order to simulate a disruption self-consistently, the initial distributions above (section 5.1) are evolved with an exponential drop in temperature, corresponding to the thermal quench in a tokamak. As the resistivity ρ increases with $T^{-3/2}$, an electric field is induced (Lenz's law), trying to maintain the initial current I_p. Given the right circumstances, a large enough electric field may be induced, which is capable of driving REs. The circumstances are favored by a short timescale of the temperature drop and a high initial temperature & current. If REs are produced during the disruption, they contribute to the total current, thereby reducing the electric field, leading to a convergence in post-disruptive current. Eventually, the total post-disruption plasma current can be driven by runaways, which is the case of a runaway beam. This runaway beam would then slowly decay with $E \approx E_c^{\text{eff}}$ [77, 68].
Mathematically, the the induction of the electric field due to a change in the plasma current can be explained by looking at the loop voltages present in a tokamak. Apart from an externally given loop-voltage U_{ex}, which is driven by a change in magnetic flux through the central solenoid (see figure 1), a self-induced voltage is present,

$$U_{\text{self}} = -L\frac{dI_p}{dt},$$

where, for a toroidal conductor and a completely homogeneous current density the inductance L is approximated by

$$L = \mu_0 R\left[\ln\left(8\frac{R}{a}\right) - 2\right].$$

Here, μ_0 is the vacuum permeability, R and a are the major and minor radius of the tokamak, respecively. Now, since the electric field and the overall loop-voltage are connected via

$$U = U_{\text{ex}} + U_{\text{self}} = 2\pi RE,$$

the electric field strength is bound to the time-derivative of the plasma current I_p. Eventually the electric field is given by

$$E = \frac{-\pi a^2 L}{2\pi R}\frac{dj}{dt} + \frac{U_{\text{ex}}}{2\pi R} \tag{24}$$

with the current density $j = I_p/(\pi a^2)$. This process is self-inductive when assuming the plasma to follow Ohm's law $j = E/\rho$. The exact solution to eq.(24) is

$$E = \frac{U_{\text{ex}}}{2\pi R} + \tilde{C}\exp\left(-\frac{t\rho a^2}{2LR}\right)$$

with some constant $\tilde{C}$. It resembles the solution of an electric circuit with the effective resistivity $\rho_{\text{eff}} = \rho a^2/2R$.

In CODE, the inductance is normalized as

$$L_{\text{CODE}} = L\frac{e^2 n_e A}{2m_e R\pi^{5/2}} \tag{25}$$

with the plasma cross-section A. This has to be remembered for calculations with time-dependent densities, as the normalized inductance becomes time-dependent. Assuming $A = \pi a^2$, the inductance for AUG ($R = 1.65$ m, $a = 0.5$ m) is $L_{\text{AUG}} = 6.6\mu H$.

The self-consistent module in CODE has been implemented recently by the main development team, and the details of the implementation are currently being written up for a publication. The main complication when evolving the kinetic equation with a self-consistent electric field is that any explicit time advance scheme will become unconditinally unstable. To numerically work around this issue it becomes necessary to solve for the distribution and the electric field at the same time. Consequently, time-advance can no longer be obtained by single matrix inversion (see section 3.1), but instead requires Newton's iteration method, significantly elevating computational power demand. For a simple benchmarking calculation using

$$N_y = 500, \quad N_\xi = 50, \quad y_{\max} = 10, \quad t_{\max} = 10\ [1/\nu_{\text{ee}}], \quad dt = \frac{t_{\max}}{100},$$

the computational time on a standard double-core desktop pc is 2.8 s in time-dependent mode, which increases to 118.7 s in self-consistent treatment with one Newton iteration step during time-advance. For respectively two and three iteration steps, the computation time is 235.0 s and 390.1 s. The number of iterations required to get a numerically converged electric field response will become as high as 3 for the disruption calculations to come.

Self-consistent electric field calculations with CODE

Using the self-consistent electric field module of CODE, the three initial distributions ($T_{e0} = [1, 2.5, 5]$ keV) will undergo a temperature drop to 1 eV without an external electric field, for $L = L_{\text{AUG}}$ and a temperature decay time of $\tau_0 = 0.25$ ms. As the externally driven loop voltage is small compared to the self-induced one, in order to reduce the number of free parameters, it is set to $E_{\text{ext}} = 0$ throughout this thesis. Roughly resembling the density evolution (from MGI) from AUG shot#33108 (figure 4) the electron density will be increased linearly in time. This actually reduces complexity of the

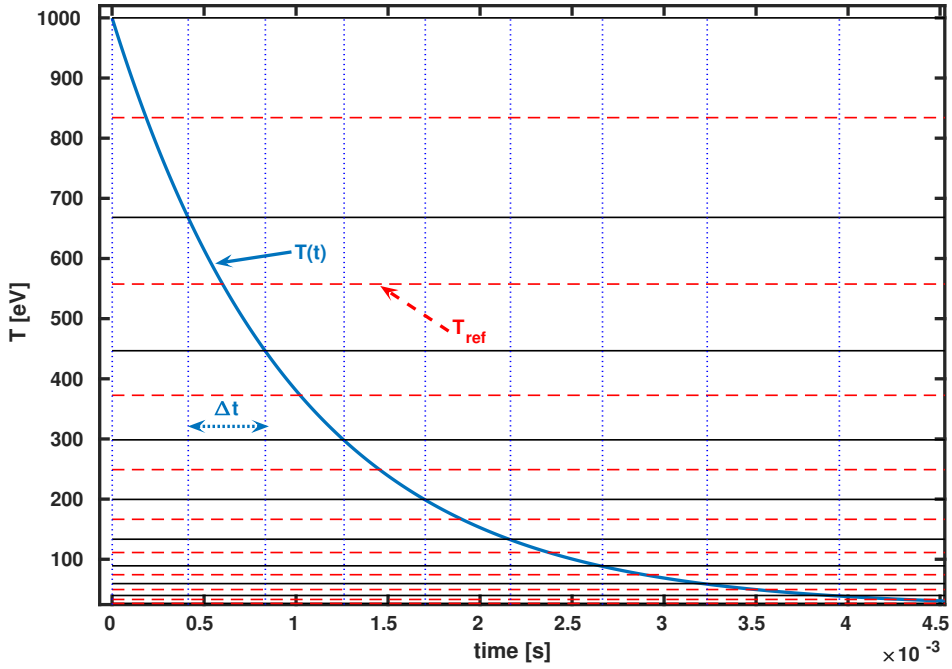

Figure 23: Exponential temperature drop $T(t)$, stepwise being chopped into time-steps Δt to respectively choose new T_{ref} for CODE restart with the previous distribution. $N_{\text{restart}} = 9$.

simulation, as the rise in density is expected to mitigate RE generation and therefore reduce the grid sizes required.

In these particular runs, I have implemented the following restart procedure (necessary to keep the reference temperature close to the instantaneous one). With N_{restart} I introduce the number of restarts during the simulation of the thermal quench. This number determines the amount of equidistant points in log$T(t)$. During the according time period Δt, the temperature is set to $T(t)$ while the reference temperature is chosen to be the mean. An example of this is illustrated in figure 23 for $N_{\text{restart}} = 9$. As the density is chosen time-dependently and is also a reference value, same restart procedure is undergone for it. For the disruption simulations to come, the number of restarts ranges from 200 to 400. With the generally demanding self-consistency of the calculations and multiple grid extensions, simulations take several days on the "TOKB" cluster nodes, which have 48 CPUs and 1 GB of system memory each. The restarting procedure also bears the advantage, that an ongoing calculation showing errors does not have to be redone all over again, but can instead be restarted from a valid state with e.g. increased numerical parameters or different operators. This is especially of interest for these self-consistent runs, because occurring errors are likely to be carried through the rest of the calculation due to the nature of the approach.

With the expectations that the CODE calculations will presumably break down at some point, the three modeled disruptions are paragraphed in the following. All simulations

are undergone with the Chiu source operator, the mean force bremsstrahlung operator and the combined linearized collision operator. Modeling the cases had been a challenge regarding numerical parameters. Due to the self-consistent calculation being generally so demanding, time and space resolution had to be kept as low as possible. For every restart, the provided "new" initial distribution had to be reshaped onto the grid due to the change in temperature, which can be done in a scripted way, but not always suited for the temperature scope given here. Oftentimes the grid had to be adjusted manually. The aforementioned problems with the bulk (see figure 22(e-f)) could often not be resolved by increasing the resolution.

1 keV thermal quench

The results obtained from a 2 ms simulation of a 1 keV disruption are depicted in figure 24. The electric field reaching values of roughly 10 [V/m] (figure 24d) are similar to the electric field values obtained by GO (see section 5.3). They are not expected to match, as GO includes the radial dependence and the radial dissipation of the electric field. Without external fields, the induced electric field is proportional to the negative of the time-derivative of the current (eq.(24)) and matches the expected trend. As seen in the time-evolution of the distribution (figure 24e) and in figure 24c, no fast particles have been generated. A certain amount of fast particles is observed in the first ms, but this is due to the fact that in the beginning, the bulk partly meets the condition for fast particles ($v > 0.25c \approx p_{\|} = 0.25$). One can see the distribution collapsing over time, while a small tail is dragged out towards higher energies. Yet the only generation of fast particles takes place at 0.3 ms$< t <$ 0.5 ms ($n_{\text{fast}} \approx 10^{-6}$), before succumbing to the effect of increasing density and energy losses. The current (figure 24d) is therefore expected to collapse completely after that, as shown previously in figure 20 and on a similar timescale ($\sim 1\ ms$). However this is not the case. The initial current depreciates only by roughly 5% and saturates, when the calculation is continued after 2 ms (not included in figure). Negative back-tails were again observed (seen as missing parts of the distribution) during calculation, but could not be dispelled. Beginning at roughly $t \approx 1.2$ ms the bulk of the distribution rises above $F = 1$. As seen in the final distribution function (figure 24f), the main bulk around $p = 0$ becomes negative, lifting its surroundings due to density conservation. This is found to be the culprit for the wrongly maintaining current.

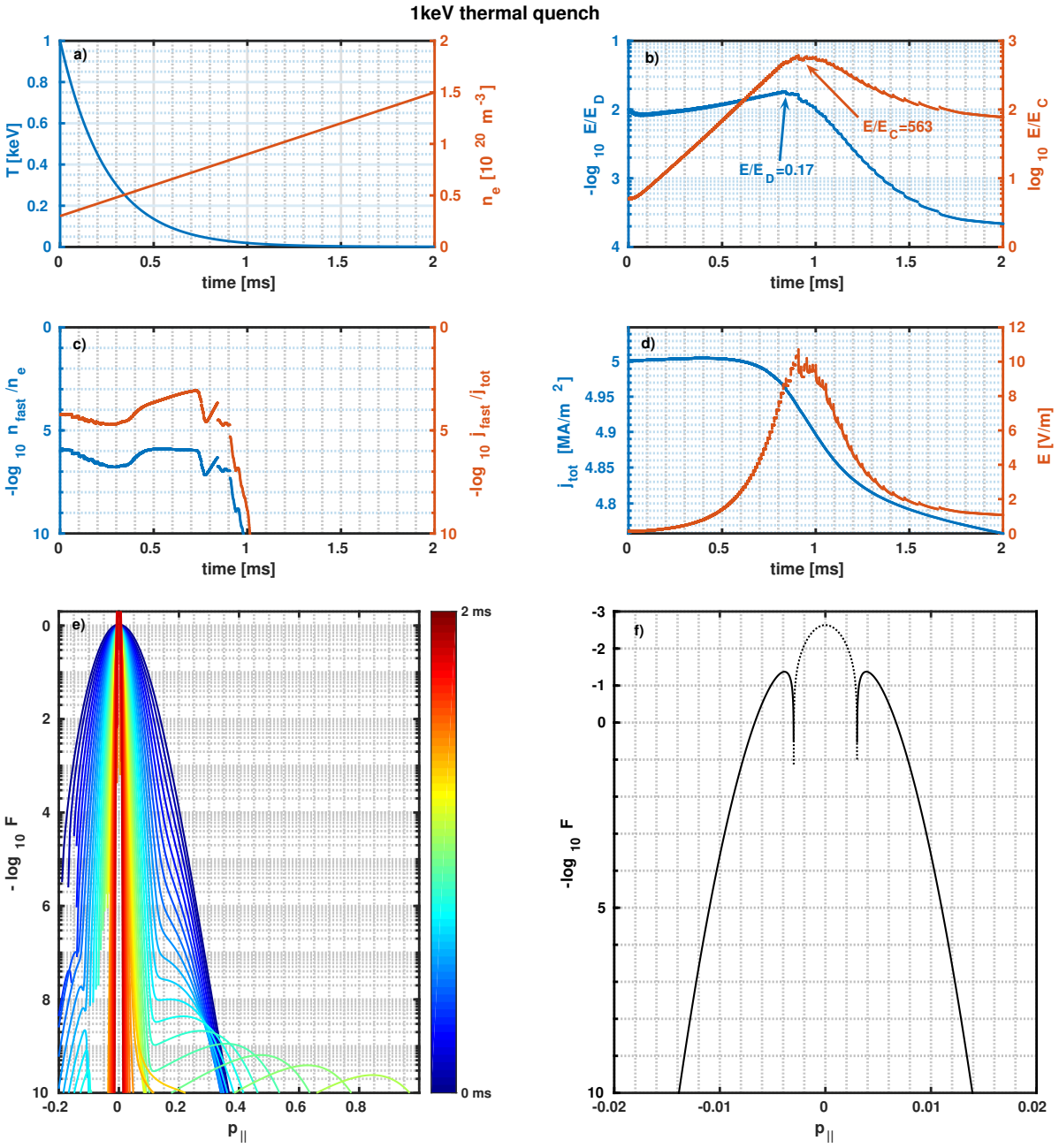

Figure 24: Simulation of a temperature drop from 1 keV to 1 eV in 2 ms with increasing density (a). (b) Shows normalized electric fields, (c) fraction of number density and current density carried by fast particles, and (d) the evolution of the total current density j_{tot} and the electric field induced. The time-evolution of the distribution function is indicated by a colorbar in (e) and (f) illustrates the last distribution of the simulation, with the negative values represented by dotted lines. Input parameters are $B = 3$ T, $Z = 1$, $E_{\mathrm{external}} = 0$, $N_{\mathrm{restart}} = 150$ and the number of Newton iteration steps is 2. Resolution parameters are adjusted during calculation and reach final values of $N_y = 4000$, $N_\xi = 30$, $y_{\mathrm{max}} = 20$.

2.5 keV thermal quench

For the initial temperature of $T_i = 2.5$ keV, the disruption simulation is represented in figure 25. Because the exponential decay time is the same as in the 1 keV-case, but the initial temperature is higher, the electric field response (figure 25d) is delayed compared to prior case. This generates a generally flatter E/E_D profile (figure 25b).
Compared to the 1 keV drop case, the amount of fast particles generated is around an order of magnitude higher $n_{\text{fast}}(0.6 \text{ ms} < t < 1 \text{ ms}) \approx 3{\cdot}10^{-5}$ (figure 25c). As before, the number density of fast particles in the beginning of the calculation is due to the bulk meeting the definition conditions of fast particles. Yet, since the current density fraction $j_{\text{fast}}/j_{\text{tot}}(0.6 \text{ ms} < t < 1 \text{ ms})$ shows a maximum of 3% in that time period, it cannot explain how the current (figure 25d) can be maintained at 95% of its original value. The same issue with negative back-tails and growing distributions is observed again. To prove that the bulk is responsible for the unphysical results, I set y_{max} constant. Shown in figure 25e is how the tail of fast particles, that was generated during the drop, leaves the computational domain and is no longer accounted for. In the same time-period, the current density drops by Δj_{tail} from 4.83 [MA/m^2] to 4.715 [MA/m^2], corresponding to 2.4%.

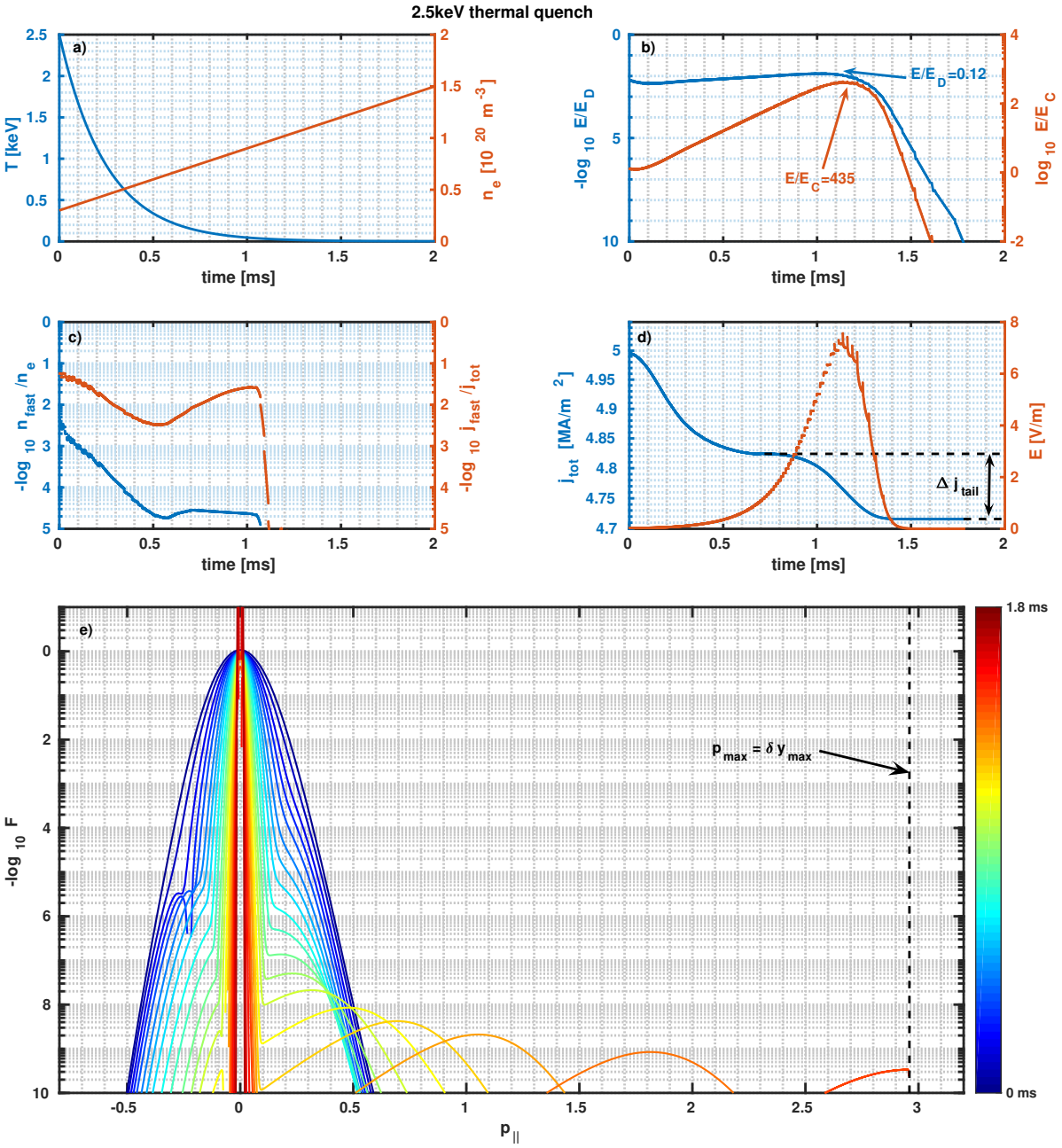

Figure 25: Simulation of a temperature drop from 2.5 keV to 1 eV in 1.8 ms with increasing density (a). (b) Shows normalized electric fields, (c) fraction of number density and current density carried by fast particles, and (d) the evolution of the total current density j_{tot} and the electric field induced. The time-evolution of the distribution function is indicated by a colorbar in (e). Input parameters are $B = 3$ T, $Z = 1$, $E_{\mathrm{external}} = 0$, $N_{\mathrm{restart}} = 290$ and the number of Newton iteration steps is 1. Resolution parameters are adjusted during calculation and reach final values of $N_y = 5700$, $N_\xi = 50$, $y_{\mathrm{max}} = 350$. p_{max} indicates the end of the computation domain.

5 keV thermal quench

The thermal quench of the $T_{e0} = 5$ keV initial distribution is shown in figure 26. The runaway tail, that is being generated in the process (figure 26e) is of considerable proportion compared to the size of the bulk, however, the linearization is not yet broken because the fast particle *density* fraction is low enough at $< 0.1\%$. Due to the non-monotonic feature in the distribution – a result of the time-evolving electric field – and the size of the tail, I used a simple, uniform grid spacing. This way, oscillations in the beginning of the tail ($p_{\|} \approx 0$) near the end of the calculations have been avoided. The fraction of fast particles (figure 26c) after 0.8 ms reaches a stable 0.1%. The continuous acceleration of the separated tail due to the electric field, converts most of the collapsing total current into fast particle current. At the end of the simulation, 93.2% of the initial 5 [MA/m^2] current density is sustained by the fast electrons (figure 26d). Prior issues with the bulk could be resolved during the calculation.
This case illustrates one possible usecase for CODE, and represent the first full quench calculation undertaken with a full-f kinetic solver for an AUG-like disruption using a self-consistent electric field. Despite the significant runaway production and almost all current carried by runaways, the calculation remained stable, with the appropriate choice of numerical parameters. The $\simeq 0.1\%$ runaway density fraction is small enough such that the linearization still holds. Therefore this present case can be considered a possible starting scenario for further investigations into AUG-like disruptions via CODE.
We have to note that the observed runaway current density conversion is high at 93.2%. A similar trend is observed for the on-axis current density when running the same case with GO. This large current conversion, in the absence of high-Z impurities in the calculation, spatial transport, or electric field diffusion, is consistent with our present understanding of runaway generation (hot-tail, Dreicer and avalanche mechanisms). For experimental comparisons, more scans will be necessary to study the effect of the aforementioned phenomena. Direct comparisons for the calculated distribution function will be possible using synthetic diagnostics (hard X-ray emission, synchrotron radiation, etc) in the future.
This work suggests that with a carefully selected set of numerical parameters, optimized resolution and a meticulous restart scheme, a full disruption cycle (thermal + current quench) can be calculated with CODE for an AUG-like set of physical paramters. As long as the runaway *number density* remains sufficiently low, the linearization does not break down. This study paves the way for further investigation into runaway generation in AUG disruptions using a linearized kinetic solver.

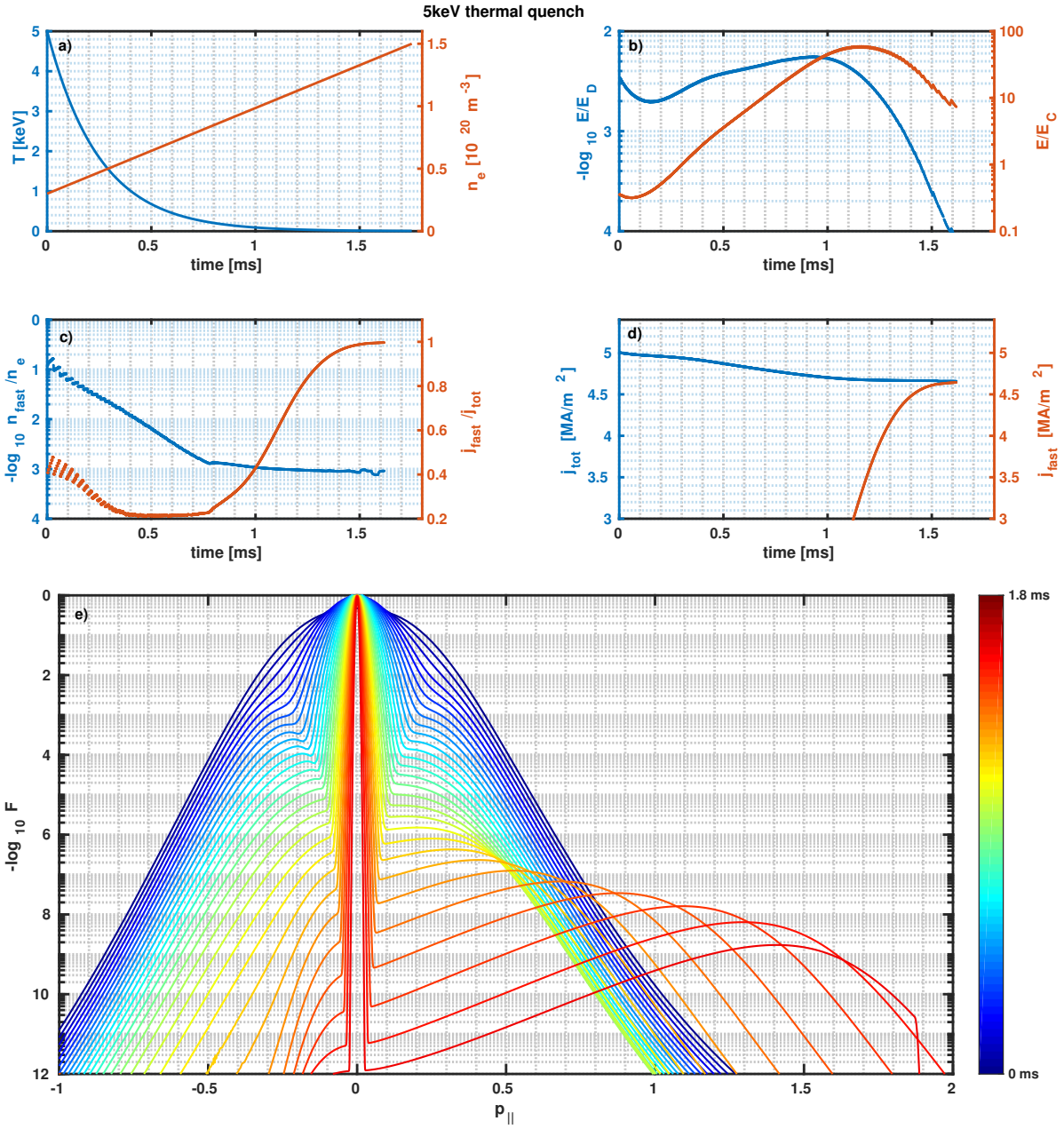

Figure 26: Simulation of a temperature drop from 5 keV to 1 eV in 1.8 ms with increasing density (a). (b) Shows normalized electric fields, (c) fraction of number density and current density carried by fast particles, and (d) the evolution of the total current density j_{tot} and fast fast current density j_{fast}. The time-evolution of the distribution function is indicated by a colorbar in (e). Input parameters are $B = 3$ T, $Z = 1$, $E_{\mathrm{external}} = 0$, $n_{\mathrm{restart}} = 300$ and the number of Newton iteration steps is 2. Resolution parameters are adjusted during calculation and reach final values of $N_y = 6000$, $N_\xi = 40$, $y_{\max} = 300$.

6. Summary

Tokamak disruptions pose an intolerable risk to large devices such as ITER and beyond. Under some circumstances that are yet to be completely understood, disruptions may generate beams of runaway electrons (RE) with energies in the multi-MeV range. This process is of great concern for large tokamaks, where beams carrying up to several MA currents could severely damage the first wall if they are suddenly lost [11, 12].
The main subject of this thesis is the numerical investigation of runaway electron dynamics. After an introduction into the theory of kinetic modeling, I introduced the main tool used in this thesis, CODE ("COllisional Distribution of Electrons") [45, 46]. CODE has been widely used in the past years to study basic runaway-related phenomena [78, 68, 66, 48, 76]. After performing some basic validation and testing (which also served as a way to learn to use the solver) I have proceeded to model two different experimentally relevant scenarios.

First, I applied CODE to flap-top runaway cases on the FTU tokamak [63]. Following an extensive parameter scan study, I have concluded that using the experimentally supplied plasma parameters CODE will significantly overpredict runaway production. I have found, that due to a high sensitivity of the runaway electron generation in that parameter regime, a reduction of the mean given electric field strength by about 15% would reproduce the observed current density. Similar results are obtained with an increase of the mean effective charge. An other possible explanation to the discrepancy is runaway transport in the flat-top scenarios [70, 73, 72], where the generation rates are much lower than in post-disruption.

The second – and more complicated – case to investigate were ASDEX Upgrade post-disruption runaway beams [17]. This requires a self-consistent treatment of the electric field, which introduces numerical complications and significantly increased run times. The main question was if CODE can be applied to a medium sized tokamak disruption, and we expected the linearization to break during the course of the current quench [70]. Several cases I ran indeed ended up with numerical issues which I could not resolve given the thesis time frame. In case of a thermal quench simulation starting at 5 keV, I have successfully followed the complete duration of the thermal- and current quench. This case resulted in a runaway beam that carries 93.2% of the initial current density, but because the runaway number density is only about 0.1%, the linearization is not broken. This case, which is the first time a full-f Fokker-Planck solver was applied successfully for a whole AUG disruption using self-consistent electric field, can serve as the basis of research into better understanding runaway dynamics on AUG.

7. Outlook

Due to the advantage of the relatively low computational cost of CODE, it is of interest to be able to simulate as much as possible using this linearized, 0D tool. Although more complete models are available and are under active development (such as the 1D LUKE [18] or the fully nonlinear relativistic solver NORSE [30, 31]), detailed and large-scale parameter scans require fast runs where CODE can hold an advantage.

One of the possible extensions to CODE can be a "local transport" model. Here the radial transport of runaway electrons would be accounted for, achieving a more thorough simulation of flaptop scenarios, like the FTU case in chapter 4. For the sake of completeness, the effect of partial-screening by the Mo impurities during the FTU shot #39464 should be quantified. In order to conclude to a distribution matching the synchrotron radiation observed by the REIS system, one could set the initial values differently. In this specific case, adjusting the electric field to be just 85% of the measured value, was enough to obtain a distribution with a runaway current as in the experiment. Therefore a distribution generated with such a setting can serve as the starting point for iterative fits using synthetic diagnostics.

In the case of disruption studies, not all issues could be resolved in the time frame of this thesis work. With further adjustments it might be possible to avoid the bulk instabilities observed in the low temperature scenarios. On the other end of the temperature scale, the 10 keV case have to be investigated using NORSE. It might be possible to adjust the CODE parameters to be able to follow the evolution of this relatively high temperature case as well, which stands the closest to the typical AUG RE experiments.
The 5 keV initial temperature cases provided a nice example where CODE can be used for a full quench (thermal and current) calculation for a tokamak the size of AUG. Currently RE generation is somewhat overpredicted. This is partially because we have not yet considered the effect of argon impurities introduced by the MGI. For this effect, the recent screening model by Hesslow et al. [66, 68] will be applied in the future. Also, the effect of seed losses [75] will have to be investigated.
On a longer timescale, both 0D hybrid calculations (using NORSE [30, 31]) and coupled 1D calculations (such as coupling with GO [76]) can be considered, for a more thorough (albeit more resource-intensive) modeling.

A. Appendix

A.1. Kinetic equation

The kinetic equation for a test-particle collision operator only (see section 3.1.1, eq. (11)) can written dimensionless with the normalized electric field $\hat{E} = -eE/(m_e v_e \nu_{ee})$, the normalized time $\hat{t} = \nu_{ee} t$ and normalized source term $\hat{S} = S m_e^3 v_e^3 \pi^{3/2}/(\nu_{ee} n_e)$ as [45]

$$\begin{aligned}
&\frac{\partial F}{\partial \hat{t}} + \hat{E}\xi\frac{\partial F}{\partial y} + \hat{E}\frac{1-\xi^2}{y}\frac{\partial F}{\partial \xi} \\
&-\frac{3\sqrt{\pi}}{4}\frac{1}{y^2}\frac{\partial}{\partial y}y^2\left[\frac{\Psi(x)}{x}\frac{\partial F}{\partial y} + 2\Psi(x)F\right] \\
&-\frac{3\sqrt{\pi}}{4}\frac{1}{2xy^2}\left[Z_{eff} + \phi(x) - \Psi(x) + \frac{\delta^4 x^2}{2}\right]\frac{\partial}{\partial \xi}\left(1-\xi^2\right)\frac{\partial F}{\partial \xi} = \hat{S}.
\end{aligned} \tag{26}$$

Expanding F in Legendre polynomials $P_L(\xi)$

$$F(y,\xi) = \sum_{L=0}^{\infty} F_L(y) P_L(\xi)$$

and using the operation

$$\frac{2L+1}{2}\int_{-1}^{1} P_L(\xi)\, d\xi$$

yields the final, discretized equation

$$\begin{aligned}
&\frac{\partial F_L}{\partial \hat{t}} + \sum_{l=0}^{\infty}\{\hat{E}\left[\frac{L+1}{2L+3}\delta_{L+1,l} + \frac{L}{2L-1}\delta_{L-1,l}\right]\frac{\partial}{\partial y} \\
&+\frac{\hat{E}}{y}\left[\frac{(L+1)(L+2)}{2L+3}\delta_{L+1,l} - \frac{(L-1)L}{2L-1}\delta_{L-1,l}\right] \\
&-\frac{3\sqrt{\pi}}{4}\frac{\Psi(x)}{x}\delta_{L,l}\frac{\partial^2}{\partial y^2} - \frac{3\sqrt{\pi}}{4}\left[\frac{2\Psi(x)}{y} + \frac{dx}{dy}\frac{d\Psi}{dx}\right]\delta_{L,l} \\
&-\frac{3\sqrt{\pi}}{4}\left[\frac{1}{x}\frac{dx}{dy}\frac{d\Psi}{dy} + \frac{2\Psi(x)}{xy} - \frac{\Psi(x)}{x^2}\frac{dx}{dy} + 2\Psi(x)\right]\delta_{L,l}\frac{\partial}{\partial y} \\
&+\frac{3\sqrt{\pi}}{8xy^2}\left[Z + \phi(x) - \Psi(x) + \frac{\delta^4 x^2}{2}\right]L(L+1)\delta_{L,l}\}F_l = \hat{S}_L
\end{aligned} \tag{27}$$

References

[1] European Physical Society position paper. "Energy for the future - EPS position paper on the nuclear option" (2007). URL: http://archive.iupap.org/epspositionpaper.pdf.

[2] J. Wesson and D.J. Campbell. *Tokamaks*. International Series of Monogr. OUP Oxford, 2011. ISBN: 9780199592234. URL: https://books.google.de/books?id=BH9vx-iDI74C.

[3] F. Chen. *An Indispensable Truth: How Fusion Power Can Save the Planet*. Springer New York, 2011. ISBN: 9781441978202. URL: https://books.google.de/books?id=D2CZf0nmKq8C.

[4] C. F. V. Weizsäcker. "Zur Theorie der Kernmassen". *Zeitschrift fur Physik* 96 (July 1935), pp. 431–458. DOI: 10.1007/BF01337700.

[5] U. Stroth. *Plasmaphysik: Phänomene, Grundlagen, Anwendungen*. Vieweg+Teubner Verlag, 2011. ISBN: 9783834883261. URL: https://books.google.de/books?id=wkEpBAAAQBAJ.

[6] T.C. Hender et al. "Chapter 3: MHD stability, operational limits and disruptions". *Nuclear Fusion* 47.6 (2007), S128. URL: http://stacks.iop.org/0029-5515/47/i=6/a=S03.

[7] B.B. Kadomtsev. "Behaviour of disruptions in Tokamaks". *Plasma Physics and Controlled Fusion* 26.1A (1984), p. 217. URL: http://stacks.iop.org/0741-3335/26/i=1A/a=320.

[8] S. E. Kruger, D. D. Schnack, and C. R. Sovinec. "Dynamics of the major disruption of a DIII-D plasma". *Physics of Plasmas* 12.5 (2005), p. 056113. DOI: 10.1063/1.1873872. eprint: https://doi.org/10.1063/1.1873872. URL: https://doi.org/10.1063/1.1873872.

[9] A. Kallenbach et al. "Scrape-off layer radiation and heat load to the ASDEX Upgrade LYRA divertor". *Nuclear Fusion* 39.7 (1999), p. 901. URL: http://stacks.iop.org/0029-5515/39/i=7/a=307.

[10] H. Dreicer. "Electron and Ion Runaway in a Fully Ionized Gas. I". *Phys. Rev.* 115 (2 1959), pp. 238–249. DOI: 10.1103/PhysRev.115.238. URL: https://link.aps.org/doi/10.1103/PhysRev.115.238.

[11] E. M. Hollmann et al. "Status of research toward the ITER disruption mitigation system". *Physics of Plasmas* 22 (2 2015), p. 021802. ISSN: 1070-664X. URL: http://dx.doi.org/10.1063/1.4901251.

[12] M. Lehnen et al. "Disruptions in ITER and strategies for their control and mitigation". *Journal of Nuclear Materials* 463 (2015), pp. 39 –48. ISSN: 0022-3115. DOI: http://dx.doi.org/10.1016/j.jnucmat.2014.10.075. URL: http://www.sciencedirect.com/science/article/pii/S0022311514007594.

[13] C. Reux et al. "Runaway electron beam generation and mitigation during disruptions at JET-ILW". *Nuclear Fusion* 55.9 (2015), p. 093013. URL: http://stacks.iop.org/0029-5515/55/i=9/a=093013.

[14] B. Esposito et al. "Avoidance of disruptions at high β N in ASDEX Upgrade with off-axis ECRH". *Nuclear Fusion* 51.8 (2011), p. 083051. URL: http://stacks.iop.org/0029-5515/51/i=8/a=083051.

[15] B. Esposito et al. "Disruption avoidance by means of electron cyclotron waves". *Plasma Physics and Controlled Fusion* 53.12 (2011), p. 124035. URL: http://stacks.iop.org/0741-3335/53/i=12/a=124035.

[16] Allen H. Boozer. "Theory of runaway electrons in ITER: Equations, important parameters, and implications for mitigation". *Physics of Plasmas* 22.3 (2015), p. 032504. DOI: 10.1063/1.4913582. eprint: https://doi.org/10.1063/1.4913582. URL: https://doi.org/10.1063/1.4913582.

[17] G. Pautasso et al. "Disruption mitigation by injection of small quantities of noble gas in ASDEX Upgrade". *Plasma Physics and Controlled Fusion* 59.1 (2017), p. 014046. URL: http://stacks.iop.org/0741-3335/59/i=1/a=014046.

[18] Decker J and Peysson Y. *DKE: A fast numerical solver for the 3D drift kinetic equation*. Euratom-CEA Report EUR-CEA-FC-1736. 2004.

[19] Marshall N. Rosenbluth, William M. MacDonald, and David L. Judd. "Fokker-Planck Equation for an Inverse-Square Force". *Phys. Rev.* 107 (1 1957), pp. 1–6. DOI: 10.1103/PhysRev.107.1. URL: https://link.aps.org/doi/10.1103/PhysRev.107.1.

[20] O Embréus, A Stahl, and T Fülöp. "Effect of bremsstrahlung radiation emission on fast electrons in plasmas". *New Journal of Physics* 18.9 (2016), p. 093023. URL: http://stacks.iop.org/1367-2630/18/i=9/a=093023.

[21] S. Chapman and T.G. Cowling. *The Mathematical Theory of Non-uniform Gases: An Account of the Kinetic Theory of Viscosity, Thermal Conduction and Diffusion in Gases*. Cambridge Mathematical Library. Cambridge University Press, 1970. ISBN: 9780521408448. URL: https://books.google.de/books?id=Cbp5JP2OTrwC.

[22] P. Helander and D.J. Sigmar. *Collisional Transport in Magnetized Plasmas*. Cambridge Monographs on Plasma Physics. Cambridge University Press, 2005. ISBN: 9780521020985. URL: https://books.google.de/books?id=nm-V01E0H2MC.

[23] F. R. Elder et al. "Radiation from Electrons in a Synchrotron". *Physical Review* 71 (June 1947), pp. 829–830. DOI: 10.1103/PhysRev.71.829.5.

[24] Adam Stahl. "Momentum-space dynamics of runaway electrons in plasmas". PhD thesis. Charlmers University Of Technology, 2017.

[25] I. M. Pankratov. "Analysis of the synchrotron radiation spectra of runaway electrons". *Plasma Physics Reports* 25 (Feb. 1999), pp. 145–148.

[26] A. Stahl et al. "Synchrotron radiation from a runaway electron distribution in tokamaks". *Physics of Plasmas* 20.9, 093302 (Sept. 2013), p. 093302. DOI: 10.1063/1.4821823. arXiv: 1308.2099 [physics.plasm-ph].

[27] J.W. Connor and R.J. Hastie. "Relativistic limitations on runaway electrons". *Nuclear Fusion* 15.3 (1975), p. 415. URL: http://stacks.iop.org/0029-5515/15/i=3/a=007.

[28] S.I. Braginskii. "Transport Processes in a Plasma". *Reviews of Plasma Physics* 1 (1965), p. 205.

[29] B. Coppi et al. "Slide-away distributions and relevant collective modes in high-temperature plasmas". *Nuclear Fusion* 16.2 (1976), p. 309. URL: http://stacks.iop.org/0029-5515/16/i=2/a=014.

[30] A. Stahl et al. "NORSE: A solver for the relativistic non-linear Fokker-Planck equation for electrons in a homogeneous plasma". *Computer Physics Communications* 212 (Mar. 2017), pp. 269–279. DOI: 10.1016/j.cpc.2016.10.024. arXiv: 1608.02742 [physics.plasm-ph].

[31] A. Stahl et al. "Runaway-electron formation and electron slide-away in an ITER post-disruption scenario". *Journal of Physics: Conference Series* 775.1 (2016), p. 012013. URL: http://stacks.iop.org/1742-6596/775/i=1/a=012013.

[32] W. Pauli. *Theory of Relativity*. Dover Publications, New York, 1981.

[33] T. Fülöp and G. Papp. "Runaway Positrons in Fusion Plasmas". *Phys. Rev. Lett.* 108 (22 2012), p. 225003. DOI: 10.1103/PhysRevLett.108.225003. URL: https://link.aps.org/doi/10.1103/PhysRevLett.108.225003.

[34] G. D. Holman. "DC Electric Field Acceleration of Ions in Solar Flares". 452 (Oct. 1995), p. 451. DOI: 10.1086/176316.

[35] O. Embréus et al. "Numerical calculation of ion runaway distributions". *Physics of Plasmas* 22.5, 052122 (May 2015), p. 052122. DOI: 10.1063/1.4921661. arXiv: 1502.06739 [physics.plasm-ph].

[36] H. Smith et al. "Runaway electron generation in a cooling plasma". *Physics of Plasmas* 12.12 (2005), p. 122505. DOI: 10.1063/1.2148966. eprint: https://doi.org/10.1063/1.2148966. URL: https://doi.org/10.1063/1.2148966.

[37] H. M. Smith and E. Verwichte. "Hot tail runaway electron generation in tokamak disruptions". *Physics of Plasmas* 15.7 (2008), p. 072502. DOI: 10.1063/1.2949692. eprint: https://doi.org/10.1063/1.2949692. URL: https://doi.org/10.1063/1.2949692.

[38] Pavel Aleynikov and Boris N. Breizman. "Generation of runaway electrons during the thermal quench in tokamaks". *Nuclear Fusion* 57.4 (2017), p. 046009. URL: http://stacks.iop.org/0029-5515/57/i=4/a=046009.

[39] T. Fehér et al. "Simulation of runaway electron generation during plasma shutdown by impurity injection in ITER". *Plasma Physics and Controlled Fusion* 53.3 (2011), p. 035014. URL: http://stacks.iop.org/0741-3335/53/i=3/a=035014.

[40] Pavel Aleynikov and Boris N. Breizman. "Generation of runaway electrons during the thermal quench in tokamaks". *Nuclear Fusion* 57.4 (2017), p. 046009. URL: http://stacks.iop.org/0029-5515/57/i=4/a=046009.

[41] M.N. Rosenbluth and S.V. Putvinski. "Theory for avalanche of runaway electrons in tokamaks". *Nuclear Fusion* 37.10 (1997), p. 1355. URL: http://stacks.iop.org/0029-5515/37/i=10/a=I03.

[42] C. Reux et al. "Runaway electron beam generation and mitigation during disruptions at JET-ILW". *Nuclear Fusion* 55.9 (2015), p. 093013. URL: http://stacks.iop.org/0029-5515/55/i=9/a=093013.

[43] M. Shimada et al. "Progress in the ITER Physics Basis Chapter 1: Overview and summary". *Nuclear Fusion* 47.6 (2007), S1. URL: http://stacks.iop.org/0029-5515/47/i=6/a=S01.

[44] T. Fülöp et al. "Destabilization of magnetosonic-whistler waves by a relativistic runaway beam". *Physics of Plasmas* 13.6 (2006), p. 062506. DOI: 10.1063/1.2208327. eprint: https://doi.org/10.1063/1.2208327. URL: https://doi.org/10.1063/1.2208327.

[45] M. Landreman, A. Stahl, and T. Fülöp. "Numerical calculation of the runaway electron distribution function and associated synchrotron emission". *Computer Physics Communications* 185 (Mar. 2014), pp. 847–855. DOI: 10.1016/j.cpc.2013.12.004. arXiv: 1305.3518 [physics.plasm-ph].

[46] A. Stahl et al. "Kinetic modelling of runaway electrons in dynamic scenarios". *Nuclear Fusion* 56.11 (2016), p. 112009. URL: http://stacks.iop.org/0029-5515/56/i=11/a=112009.

[47] A. Stahl et al. "Effective Critical Electric Field for Runaway-Electron Generation". *Physical Review Letters* 114.11, 115002 (Mar. 2015), p. 115002. DOI: 10.1103/PhysRevLett.114.115002. arXiv: 1412.4608 [physics.plasm-ph].

[48] O. Embréus, A. Stahl, and T. Fülöp. "Effect of bremsstrahlung radiation emission on fast electrons in plasmas". *New Journal of Physics* 18.9, 093023 (Sept. 2016), p. 093023. DOI: 10.1088/1367-2630/18/9/093023. arXiv: 1604.03331 [physics.plasm-ph].

[49] "Towards self-consistent runaway electron modeling". *42nd European Physical Society Conference on Plasma Physics, EPS 2015*. European Physical Society (EPS).

[50] G. Papp et al. "Runaway electron drift orbits in magnetostatic perturbed fields". *Nuclear Fusion* 51.4 (2011), p. 043004. URL: http://stacks.iop.org/0029-5515/51/i=4/a=043004.

[51] Robert S. Cohen, Lyman Spitzer, and Paul McR. Routly. "The Electrical Conductivity of an Ionized Gas". *Phys. Rev.* 80 (2 1950), pp. 230–238. DOI: 10.1103/PhysRev.80.230. URL: https://link.aps.org/doi/10.1103/PhysRev.80.230.

[52] M. Bakhtiari, G. J. Kramer, and D. G. Whyte. "Momentum-space study of the effect of bremsstrahlung radiation on the energy of runaway electrons in tokamaks". *Physics of Plasmas* 12.10 (2005), p. 102503. DOI: 10.1063/1.2065368. eprint: https://doi.org/10.1063/1.2065368. URL: https://doi.org/10.1063/1.2065368.

[53] M. Bakhtiari, G. J. Kramer, and D. G. Whyte. "Momentum-space study of the effect of bremsstrahlung radiation on the energy of runaway electrons in tokamaks". *Physics of Plasmas* 12.10 (2005), p. 102503. DOI: 10.1063/1.2065368. eprint: https://doi.org/10.1063/1.2065368. URL: https://doi.org/10.1063/1.2065368.

[54] O. Oxenius. *Kinetic Theory of Particles and Photons*. Springer, 1986. ISBN: 978-3-642-70728-5. DOI: 10.1007/978-3-642-70728-5.

[55] S.C. Chiu et al. "Fokker-Planck simulations mylb of knock-on electron runaway avalanche and bursts in tokamaks". *Nuclear Fusion* 38.11 (1998), p. 1711. URL: http://stacks.iop.org/0029-5515/38/i=11/a=309.

[56] O. Embréus, A. Stahl, and T. Fülöp. "On the relativistic large-angle electron collision operator for runaway avalanches in plasmas". *Journal of Plasma Physics* 84.1, 905840102 (Feb. 2018), p. 905840102. DOI: 10.1017/S002237781700099X. arXiv: 1708.08779 [physics.plasm-ph].

[57] E. Nilsson et al. "Kinetic modelling of runaway electron avalanches in tokamak plasmas". *Plasma Physics and Controlled Fusion* 57.9 (2015), p. 095006. URL: http://stacks.iop.org/0741-3335/57/i=9/a=095006.

[58] J. Decker et al. "Numerical characterization of bump formation in the runaway electron tail". *Plasma Physics and Controlled Fusion* 58.2 (2016), p. 025016. URL: http://stacks.iop.org/0741-3335/58/i=2/a=025016.

[59] Russell M. Kulsrud et al. "Runaway Electrons in a Plasma". *Phys. Rev. Lett.* 31 (11 1973), pp. 690–693. DOI: 10.1103/PhysRevLett.31.690. URL: https://link.aps.org/doi/10.1103/PhysRevLett.31.690.

[60] *FTU website*. http://ftu.frascati.enea.it. Accessed: 2018-04-3.

[61] G. Ferro, (...), A. Lier, et al. "Adaptive control design and energy distribution estimation via nonlinear observer for runaway electron in FTU". *Europhysics Conference Abstracts*. Vol. 41F. 2017, P5.156. URL: http://ocs.ciemat.es/EPS2017PAP/pdf/P5.156.pdf.

[62] A. Stahl et al. "Synchrotron radiation from a runaway electron distribution in tokamaks". *Physics of Plasmas* 20.9, 093302 (Sept. 2013), p. 093302. DOI: 10.1063/1.4821823. arXiv: 1308.2099 [physics.plasm-ph].

[63] B. Esposito et al. "Runaway electron generation and control". *Plasma Physics and Controlled Fusion* 59.1 (2017), p. 014044. URL: http://stacks.iop.org/0741-3335/59/i=1/a=014044.

[64] O. Embréus et al. "Effect of bremsstrahlung radiation emission on distributions of runaway electrons in magnetized plasmas". *ArXiv e-prints* (Nov. 2015). arXiv: 1511.03917 [physics.plasm-ph].

[65] T. Pütterich et al. "Modelling of measured tungsten spectra from ASDEX Upgrade and predictions for ITER". *Plasma Physics and Controlled Fusion* 50.8 (2008), p. 085016. URL: http://stacks.iop.org/0741-3335/50/i=8/a=085016.

[66] L. Hesslow et al. "Effect of Partially Screened Nuclei on Fast-Electron Dynamics". *Physical Review Letters* 118.25, 255001 (June 2017), p. 255001. DOI: 10.1103/PhysRevLett.118.255001. arXiv: 1705.08638 [physics.plasm-ph].

[67] K.B. Fournier et al. "Calculation of the radiative cooling coefficient for molybdenum in a low density plasma". *Nuclear Fusion* 38.4 (1998), p. 639. URL: http://stacks.iop.org/0029-5515/38/i=4/a=513.

[68] L. Hesslow et al. "Effect of partially ionized impurities and radiation on the effective critical electric field for runaway generation". *ArXiv e-prints* (May 2018). arXiv: 1802.00717v3 [physics.plasm-ph].

[69] G. Papp et al. "The effect of ITER-like wall on runaway electron generation in JET". *Nuclear Fusion* 53.12 (2013), p. 123017. URL: http://stacks.iop.org/0029-5515/53/i=12/a=123017.

[70] G. Papp et al. "Energetic electron transport in the presence of magnetic perturbations in magnetically confined plasmas". *Journal of Plasma Physics* 81 (05 Oct. 2015), p. 475810503. ISSN: 1469-7807. DOI: 10.1017/S0022377815000537. URL: http://journals.cambridge.org/article_S0022377815000537.

[71] T. Fehér et al. "Simulation of runaway electron generation during plasma shutdown by impurity injection in ITER". *PPCF* 53.3 (2011), p. 035014. URL: http://stacks.iop.org/0741-3335/53/i=3/a=035014.

[72] J. Decker et al. "Runaway Electron Physics and Modelling". EUROfusion Science Meeting. 2017.

[73] T. Hauff and F. Jenko. "Runaway electron transport via tokamak microturbulence". *Physics of Plasmas* 16.10 (2009), p. 102308. DOI: 10.1063/1.3243494. eprint: https://doi.org/10.1063/1.3243494. URL: https://doi.org/10.1063/1.3243494.

[74] Konsta Sarkimaki et al. "An advection-diffusion model for cross-field runaway electron transport in perturbed magnetic fields". *Plasma Physics and Controlled Fusion* 58.12 (2016), p. 125017. URL: http://stacks.iop.org/0741-3335/58/i=12/a=125017.

[75] C. Sommariva et al. "Test particles dynamics in the JOREK 3D non-linear MHD code and application to electron transport in a disruption simulation". *Nuclear Fusion* 58.1 (2018), p. 016043. URL: http://stacks.iop.org/0029-5515/58/i=1/a=016043.

[76] G. Papp et al. “Generation and suppression of runaway electrons in ASDEX Upgrade disruptions”. *ECA*. Vol. 39E. 2015, P1.173. ISBN: 2-914771-98-3. URL: http://ocs.ciemat.es/EPS2015PAP/pdf/P1.173.pdf.

[77] Boris N. Breizman. “Marginal stability model for the decay of runaway electron current”. *Nuclear Fusion* 54.7 (2014), p. 072002. URL: http://stacks.iop.org/0029-5515/54/i=7/a=072002.

[78] E. Hirvijoki et al. “Radiation reaction induced non-monotonic features in runaway electron distributions”. *Journal of Plasma Physics* 81.5 (2015). DOI: 10.1017/S0022377815000513.